A 3-D Nodal-Averaged Gradient Approach For Unstructured-Grid Cell-Centered Finite-Volume Methods For Application to Turbulent Hypersonic Flow

Jeffery A. White[1]
NASA Langley Research Center, Hampton, VA, 23681, USA
Hioraki Nishikawa[2]
National Institute of Aerospace, Hampton, VA, 23666, USA
Robert A. Baurle[3]
NASA Langley Research Center, Hampton, VA, 23681, USA

A 2-D nodal weighted least-squares gradient method and a related face-averaged nodal gradient approach that were developed for use with triangular grids are extended to 3-D for use with tetrahedral grids. In addition, a method, developed in 2-D, to stabilize the iterative convergence of these methods on quadrilateral cells is described and extended to 3-D and remedies are investigated to determine the nodal gradient averaging approach most suitable for use with grids made up of hexahedral, prismatic, pyramidal and tetrahedral cells. Moreover, due to an interest in hypersonic flow, a robust multidimensional gradient limiter procedure that is consistent with the stencil used to construct the nodal gradients is described. Finally, we demonstrate that the resulting 3-D methods are sufficiently robust for use in scramjet computations through the solution of three canonical turbulent hypersonic flow problems as well as a physically realistic 3-D scramjet inlet geometry.

I. Introduction

We are motivated to seek improved gradient computations by near term and long term code development goals. Our near term goals include the desire to reduce, in terms of computational effort and storage, the cost of computing gradients, and to improve the fidelity and robustness of the VULCAN-CFD code on the most common types of grid cell topologies produced by Commercial Off The Shelf (COTS) grid generation codes. Our long term goals include a need to improve the fidelity and robustness of the 2nd-order cell-centered control volume approach used in VULCAN-CFD on tetrahedral grids. This long term goal is motivated by the recognition that unstructured grid adaptation, primarily on tetrahedral grids, has the potential to be a powerful tool in the control of discretization error in Computational Fluid Dynamics (CFD) [1]. As discussed in Ref. [1] the current state-of-the-art of unstructured grid adaptation methods on tetrahedral grids can lead to grids that have highly skewed high aspect ratio cells that can make the computation of gradients challenging thereby requiring that special attention be paid to the numerics for these types of grids.

This paper is a companion to the AIAA SciTech 2020 paper "Face- and Cell-Averaged Nodal-Gradient Approach to Cell-Centered Finite-Volume Method on Mixed Grids" [2], in which a 2-D nodal-gradient or node-centered gradient approach to computing weighted least squares (WLSQ) gradients on mixed element grids is developed and described. In turn, Ref. [2] describes the 2-D mixed element extension of a triangular element face-averaged node-centered gradient approach proposed and described in Ref. [3]. The novel node-centered gradient approach in Ref. [3] was shown to have several advantages over conventional cell-centered gradient/cell-average gradient methods on triangles. These advantages were; 1) it requires less storage for least-squares gradient coefficients and gradient computations, 2) it reduces the amount of interpartition communication with respect to gradients, and 3) it reduces the size of the residual stencil. In Ref. [2] the face-averaged nodal-gradient (F-ANG) method was shown to be unstable for quadrilateral elements and an averaging of the cells nodal gradients was proposed as a remedy. In addition, a hybrid face and cell averaging of nodal gradients for 2-D mixed element grids containing both quadrilateral and triangular elements was developed. In the current work, the objective is threefold; 1) to extend the 2-D face and cell-averaged nodal-gradient approach (FAC-ANG) of Ref. [2] to 3-D for the general case of grids containing a mixture of hexahedral, pyramidal, prismatic and tetrahedral elements, 2) to determine if the advantages found in 2-D [2,3] still exist in 3-D when utilizing a parallel computing paradigm and 3) to demonstrate that the resulting method can, through the proper construction of the gradient limiter, be robust enough for use in computing high speed flows. Objective 1) will be accomplished by building on the previous work described in [5,6,7] and describing how the resulting 3-D FAC-ANG, approach and an alternative form, the face or cell-averaged nodal gradient (FOC-ANG) approach differ from the conventional face neighbors of face-neighbors cell-centered gradient (FN2-CCG) and node-neighbor cell-centered gradient (NN-CCG) approaches. Objectives 2) and 3) will be met by implementing the FAC-ANG and FOC-ANG approaches in the VULCAN-CFD [4-7] unstructured, cell-centered, finite-volume solver. Objective 3) will be met by developing a multidimensional gradient limiter procedure that is consistent with the stencil that is used to construct

[1]Aerospace Technologist, Computational AeroSciences Branch, MS 128, Associate Fellow, AIAA.
[2]Associate Research Fellow, Research Department, MS 128, Associate Fellow, AIAA.
[3]Aerospace Technologist, High Speed Airbreathing Propulsion Branch, MS 168, Associate Fellow, AIAA.

the weighted least-squares gradients at the nodes as well as the inviscid residual stencil. Finally, the relative behavior of the 3-D averaged nodal gradient approaches with respect to the cell-centered gradient approach is demonstrated through the computation of canonical hypersonic flows and the relative robustness of the approach is investigated through the computation of thermally-perfect hypersonic turbulent flow through a physically realistic 3-D scramjet component geometry.

II. Methodology

A. Role, Importance and Construction of the Gradient.

Solution gradients are perhaps the most important and one of the more difficult quantities to obtain accurately and robustly on irregular, unstructured grids. The solution gradients are required to accomplish three things when computing the residual of the discrete equations for each time step/cycle of the solution process: 1) to perform the higher-order reconstruction when computing the inviscid fluxes, 2) to compute the cell-face gradient when computing the viscous fluxes, and 3) to compute the source terms for the turbulence modeling transport equations. Moreover, there is evidence in the literature that a different definition of the cell-average gradient may be required to compute each of these quantities [8].

While no single gradient method has been found to be accurate for all arbitrary polygons, with some caveats [9], the weighted linear least-squares method has proven to be the preferred method [10,11] for node-centered and cell-centered 2nd-order finite-volume schemes. Therefore, based on the results in the literature [8-12], the weighted least-squares method was chosen in [4] as the best approach for implementation in the VULCAN-CFD unstructured grid solver. The WLSQ gradient method is based on a polynomial fit over a set of nearby data. For 2nd-order finite-volume schemes, the gradients need to be at least 1st-order accurate on general unstructured grids; and thus, it is sufficient to fit a linear polynomial. For a 2nd-order cell-centered finite-volume scheme, the authors are aware of at least three distinct ways to compute the gradient. These are to 1) compute the cell-centered gradient (CCG) directly using a cell-centered WLSQ method [5-11], 2) compute the gradients directly at the nodes, aka the nodal gradients (NG), using a node-centered WLSQ method [13-15] and then utilize some form of NG averaging to compute the averaged nodal gradients (ANG) at the cell centroid and/or the cell face centroids or 3) interpolate the cell-average solution to the nodes using a clipped pseudo-Laplacian interpolation and then compute the cell average gradient using Green-Gauss [16]. Of the three methods, we have chosen to concentrate our efforts on CCG and NG WLSQ gradient methods due to the need for clipping in the method of Ref. [16].

When faced with the need to construct gradients on unstructured hybrid grids the methodology used to construct the fluxes at the faces of the control volume directly influence how one chooses to construct the gradients. Therefore, a review of the inviscid and viscous flux construction for a 2-D hybrid grid cell face, shown in red in Fig. 1 follows.

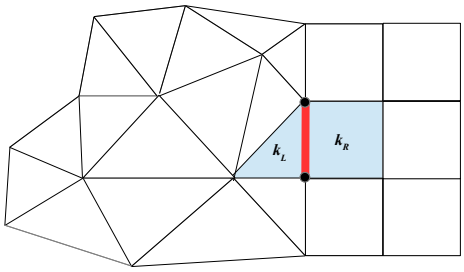

Fig. 1 2-D hybrid grid control volume interface between the triangular cell, k_L, and the quadrilateral cell, k_R.

B. Role of the Gradient in Inviscid Flux Construction

If the inviscid fluxes are computed using an upwind flux scheme, a reconstruction based 2nd-order finite-volume cell-centered scheme that utilizes an approximate Riemann solver such as the LDFSS [17] or HLLC schemes [18], requires that the inviscid flux reconstruction variables, q_i, be reconstructed at the left (L) and right (R) sides of the cell face midpoint, **X**, as shown in Fig. 2-a. The inviscid flux reconstruction variables are the cell average variables defined as

$$q_i = \left(\frac{\rho_1}{\rho},\ldots,\frac{\rho_{ncs}}{\rho},\rho,u,v,w,P,k,\omega\right) \quad \text{for thermal equilibrium, or,}$$

$$q_i = \left(\frac{\rho_1}{\rho},\ldots,\frac{\rho_{ncs}}{\rho},\rho,u,v,w,T_{ve},P,k,\omega\right) \quad \text{for thermal nonequilibrium,}$$

where $\frac{\rho_1}{\rho},\ldots,\frac{\rho_{ncs}}{\rho},\rho,u,v,w,T_{ve},P,k,\omega$ are the chemical species mass fractions, from 1 to the number of chemical species, static density, Cartesian velocity components, vibrational/electronic Temperature, static pressure, turbulent kinetic energy, and specific turbulent dissipation rate, respectively.

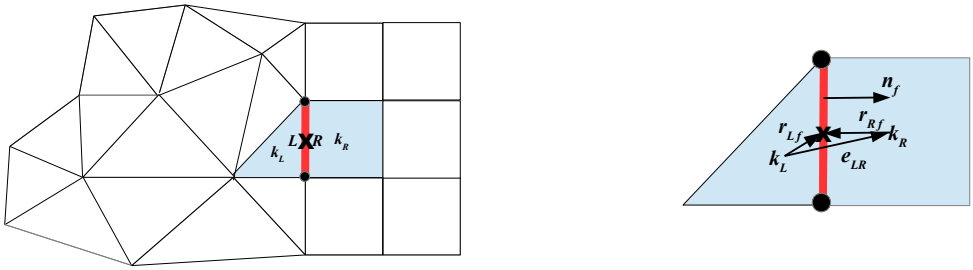

a) Reconstruction to the cell face centroid b) Reconstruction Vectors

Fig. 2 2-D reconstruction of the *L* and *R* states at the hybrid cell face, *f*, centroid, x, for the inviscid and viscous fluxes.

A 1st-order accurate scheme results when the cell-average values, q_{ik}, of the cell to the left, k_L, and the cell to the right, k_R, of the cell face are used. A 2nd-order accurate scheme results when the L and R primitive variables are reconstructed to the cell face midpoint with an extrapolation or interpolation method based on the left and right cell-average primitive variables and gradients, q_{ik_L}, q_{ik_R}, and $\overline{\nabla q_i}^L, \overline{\nabla q_i}^R$, respectively, as given by

$$q_{if}^L = q_{ik_L} + \overline{\nabla q_i}^L \cdot \vec{r_{Lf}}, \tag{1}$$

$$q_{if}^R = q_{ik_R} + \overline{\nabla q_i}^R \cdot \vec{r_{Rf}}, \tag{2}$$

where $\vec{r_{Lf}}$ and $\vec{r_{Rf}}$ are defined in Fig. 2-b. In addition to the scheme above, which is an unstructured-grid interpretation of Fromm's scheme [19], the higher-order variable extrapolation (or U-MUSCL) reconstruction scheme [20] can also be used to control the dissipation of the scheme further. The U-MUSCL scheme can be written as

$$q_{if}^L = q_{ik_L} + \frac{\chi}{2}(q_{ik_R} - q_{ik_L}) + (1-\chi)(\overline{\nabla q_i}^L \cdot \vec{r_{Lf}}) \tag{3}$$

$$q_{if}^R = q_{ik_R} + \frac{\chi}{2}(q_{ik_L} - q_{ik_R}) + (1-\chi)(\overline{\nabla q_i}^R \cdot \vec{r_{Rf}}) \tag{4}$$

where χ is used to control the behavior and the 1-D order of accuracy of the scheme when the flow is smooth.

1. $\chi = 0$, gives Fromm's scheme,
2. $\chi = -1$, gives a 2nd-order fully upwind MUSCL-type scheme,
3. $\chi = 1/3$, gives a 3rd-order upwind biased MUSCL-type scheme.

C. Role of the Gradient in Viscous Flux Construction.

The computation of the viscous flux requires that the cell-face average viscous primitive variable, $\overline{q_{v,f}}$, and the cell-face average gradient of the viscous primitive variables, $\overline{\nabla q_{v,f}}$, be computed, where the viscous primitive variables are,

$$q_{v,f} = (\frac{\rho_1}{\rho}, \ldots, \frac{\rho_{ncs}}{\rho}, \rho, u, v, w, T, k, \omega) \quad \text{for thermal equilibrium, or,}$$

$$q_{v,f} = (\frac{\rho_1}{\rho}, \ldots, \frac{\rho_{ncs}}{\rho}, \rho, u, v, w, T_{ve}, T_{tr}, k, \omega) \quad \text{for thermal nonequilibrium,}$$

with T, T_{ve} and T_{tr} being the static, vibrational/electronic and translational/rotational temperatures, respectively. We have found that the construction of $\overline{q_{vf}}$, should be consistent with the method used to compute the cell face gradient of the primitive variable, therefore, we begin by describing the methods that can be used to construct the cell face gradient. Hasselbacher [21] observed that computing $\overline{\nabla q_{vf}}$ as a simple average of the left and right face gradients, i.e.,

$$\overline{\nabla q_{vf}} = \frac{(\overline{\nabla q_v}^L + \overline{\nabla q_v}^R)}{2}, \tag{5}$$

leads to odd-even decoupling necessitating the introduction of face-derivative augmentation. Hasselbacher suggested two methods to accomplish this augmentation: aka the edge-normal (*EN*) and face-tangent (*FT*) cell-face gradient augmentation methods. The edge-normal and face-tangent augmented cell-face gradient methods were studied in Refs. [4,8,22], where the face-tangent method was found to be preferable to the edge-normal method. Moreover, in Ref. [8], the observation was made that, in many cases, a converged solution could only be obtained when the face-tangent augmented face-gradient method was used. Therefore, since the edge-normal augmented cell-face gradient method does

not result in a robust method on skewed grids it is not considered further. In a cell-centered context, we define the cell-face viscous primitive variable and face-tangent augmented cell-face gradient, $\widehat{\nabla q}_{vf}^{FT}$, and $\overline{q_{vf}}$, respectively as

$$\overline{q_{vf}} = \frac{(q_{vk_L}+q_{vk_R})}{2} \text{ and } \widehat{\nabla q}_{vf}^{FT} = \overline{\nabla q}_{vf} - [(\overline{\nabla q}_{vf} \cdot \hat{e}_{LR}) - \frac{(q_{vk_R} - q_{vk_L})}{|\vec{e}_{LR}|}](\frac{\hat{n}_f}{\hat{n}_f \cdot \hat{e}_{LR}}) \quad , \tag{6}$$

where q_{vk_L} and q_{vk_R} are the left and right cell viscous primitive variables, $\hat{n}_f$, is the cell face unit normal vector, and the vector connecting the left and right cell centroids, $\vec{e}_{LR}$ and its unit vector $\hat{e}_{LR}$ are defined in Fig. 2-b. More recently, Nishikawa [24] proposed a new approach where the cell face gradient construction approach is derived from an advection scheme applied to a hyperbolic diffusion model. The resulting viscous diffusion scheme has a consistent approximation term and an adjustable high-frequency damping term with a coefficient alpha, and thus is referred to as the alpha-damping scheme. Nishikawa considers the Hasselbacher augmentation terms, the bracketed terms in Eq. (6), to be damping terms. Furthermore, Nishikawa makes the observation that this damping term is why the face-tangent method is a robust scheme on highly skewed meshes. He attributes this robustness to the face-tangent schemes dependence on the cell skewness term, $1/(\hat{n}_f \cdot \hat{e}_{LR})$, because as skewness increases, $(\hat{n}_f \cdot \hat{e}_{LR})$ decreases, thereby increasing damping. When Nishikawa's hyperbolic diffusion-based approach [24] is applied to a cell-centered, finite-volume scheme, it results in a reconstruction-based cell-face average gradient, $\widehat{\nabla q}_{vf}^{AD}$, that includes a damping term that arises naturally due to an upwind method being used to discretize the construction of the cell-face average gradient. In this reconstruction based cell-face average gradient method, aka, the alpha-damping scheme, $\overline{q_{vf}}$, and $\widehat{\nabla q}_{vf}^{AD}$, have the form

$$\overline{q_{vf}} = \frac{(q_{vf}^L+q_{vf}^R)}{2} \text{ and } \widehat{\nabla q}_{vf}^{AD} = \overline{\nabla q}_{vf} + \alpha(\frac{\hat{n}_f}{|\vec{e}_{LR} \cdot \hat{n}_f|})\ (q_{vf}^R - q_{vf}^L) \quad , \tag{7}$$

where α is a damping coefficient and q_{vf}^L and q_{vf}^R are the left and right higher-order-reconstructed viscous face state variables. These state variables are reconstructed using Fromm's scheme where

$$q_{vf}^L = q_{vk_L} + \overline{\nabla q}_v^L \cdot \vec{r_{Lf}}, \tag{8}$$

$$q_{vf}^R = q_{vk_R} + \overline{\nabla q}_v^R \cdot \vec{r_{Rf}}. \tag{9}$$

The first term in Eq. (7) is the consistent term approximating the face gradient, and the second term is the adjustable damping term. Observe that the alpha-damping scheme reduces to the face-tangent method when 1) the reconstruction is performed halfway between the two centroids across the face, instead of at the face, 2) the absolute value is removed from the skewness measure in the denominator and 3) α=1.

D. Construction of Gradients for Inviscid Flux, Viscous Flux and Source Terms.

Equations (1-9) show that the inviscid and viscous fluxes require that left and right gradients, $\overline{\nabla q}_i^L, \overline{\nabla q}_v^L, \overline{\nabla q}_i^R$, and $\overline{\nabla q}_v^R$ of the inviscid and viscous primitive variables be computed. Moreover, the computation of turbulent flow requires the computation of cell average gradients of the viscous primitive variables for the construction of the turbulence model source terms. Therefore, a discussion regarding possible approaches using the WLSQ method to compute these gradients, follows.

D.1. Cell-centered weighted least-squares gradients using a cell-centered solution.

The state of the art for the direct computation of cell-centered gradients has been the subject of extensive research [4-12]. For a detailed description of the most popular cell average gradient WLSQ methods as well as a recently developed method based on analysis of the least-squares coefficient matrix the reader is directed to Refs. [4 -7]. In the current work, we will consider the most popular cell average gradient stencils. These are the face neighbor of face neighbors (FN2-CCG) and node neighbor (NN-CCG) cell-centered gradient stencils illustrated in Fig. 3 and Fig. 4 respectively.

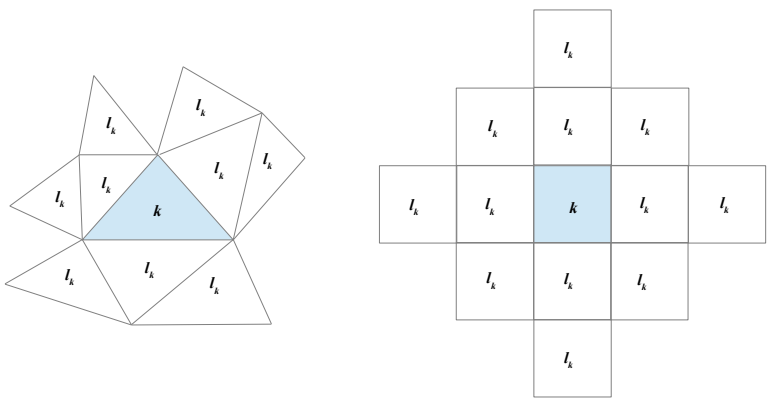

Fig. 3 The 2-D FN2-CCG WLSQ stencil, $\{l_k\}$, for cell, k (blue shaded area), on representative triangular and quadrilateral grids.

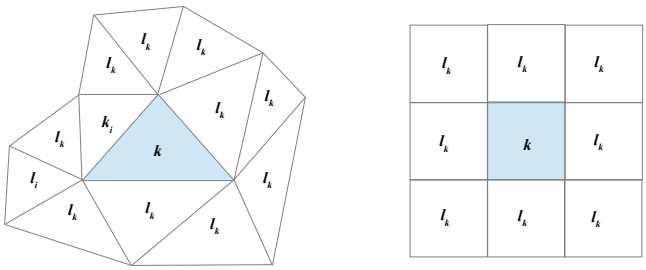

Fig. 4 The 2-D NN-CCG WLSQ stencil, $\{l_k\}$, cell, k (blue shaded area), on representative triangular and quadrilateral grids.

D.2. Node-centered weighted least-squares gradients using a cell-centered cell-average solution.

Zhang [13-15] proposed a WLSQ 2-D method where the gradients are computed at the nodes and averaged to the cells. Figure 5 presents the stencils required to define the gradients at the nodes, $j=1, 2, \ldots, N_{cell(k)}^{nodes}$ for a cell, k, where, $N_{cell(k)}^{nodes}$, is the number of nodes that surround cell k, on grids made up of triangular and quadrilateral control volumes, respectively. These nodal gradients can, in turn, be used to construct face-averaged nodal gradients (F-ANG), and the cell-averaged nodal gradients (C-ANG) [2,3]. To compute the gradient of a solution variable q at a node, j, we use the set, $\{l_j\}$ of $N \geq 3$, of the nearby cells that share the node (i.e., a gradient stencil). It is important to note that the

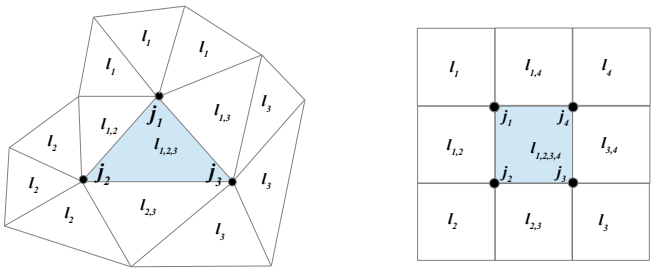

Fig. 5 The 2-D stencils $\{l_i\}$, for computing the WLSQ gradients at the nodes $j=1, 2, \ldots, N_{cell(k)}^{nodes}$ for cell, k (blue shaded area), on representative triangular and quadrilateral grids.

solution values are not available at the nodes because numerical solutions are stored at cells in the cell-centered finite-volume method. Which, as pointed out by Zhang [13-15], requires the inclusion of the solution value at the node as an additional unknown when formulating the least-squares problem. Therefore, because we are ultimately interested in 3-D, we fit a linear polynomial over $\{l_j\}$ such that:

$$q_l = q_j + \overline{\partial_x q_j}(x_l - x_j) + \overline{\partial_y q_j}(y_l - y_j) + \overline{\partial_z q_j}(z_l - z_j) \quad , \quad l \in \{l_i\}, \tag{10}$$

where, $j \in \{l_i\}$, (x_j, y_j, z_j) and (x_l, y_l, z_l) denote the coordinates of the node, j, and the set of neighbor cells, l, respectively, and q_j, $\overline{\partial_x q_j}$, $\overline{\partial_y q_j}$, $\overline{\partial_z q_j}$ is the solution vector containing the solution and derivative that we wish to compute at node j. To determine the unknowns, we need at least three and four cells around the node in 2-D and 3-D, respectively. For interior nodes, such as shown in Fig. 5, there are always sufficient cells available for the LSQ problem to be solved. However, at boundary nodes, as shown in Ref. [2], the stencil size may result in an underdetermined LSQ problem. In the current work we follow he approach described in Ref. [2]. However, the best way to augment the stencil remains and open area of research. Following Zhang [13-15], we employ the WLSQ formulation:

$$Ax = b, \tag{11}$$

where

$$A = \begin{bmatrix} w_1^n & w_1^n(x_1 - x_j) & w_1^n(y_1 - y_j) & w_1^n(z_1 - z_j) \\ \vdots & \vdots & \vdots & \vdots \\ w_l^n & w_l^n(x_l - x_j) & w_l^n(y_l - y_j) & w_l^n(z_l - z_j) \\ \vdots & \vdots & \vdots & \vdots \\ w_{N_{node(j)}^{cells}}^n & w_{N_{node(j)}^{cells}}^n(x_{N_{node(j)}^{cells}} - x_j) & w_{N_{node(j)}^{cells}}^n(y_{N_{node(j)}^{cells}} - y_j) & w_{N_{node(j)}^{cells}}^n(z_{N_{node(j)}^{cells}} - z_j) \end{bmatrix}, \quad x = \begin{bmatrix} q_j \\ \overline{\partial_x q_j} \\ \overline{\partial_y q_j} \\ \overline{\partial_z q_j} \end{bmatrix}, \quad b = \begin{bmatrix} w_1^n q_1 \\ \vdots \\ w_l^n q_l \\ \vdots \\ w_{N_k}^n q_{N_{node(j)}^{cells}} \end{bmatrix}, \tag{12}$$

$N_{node(j)}^{cells}$ is the number of cells that surround node j and w_l^n is the weight applied to the equation corresponding to the neighbor cell l. The following inverse-distance weight is widely used in finite-volume methods:

$$w_l^n = \frac{1}{d_l^{p(n)}} \quad , \quad d_l = \sqrt{(x_l - x_j)^2 + (y_l - y_j)^2 + (z_l - z_j)^2} \quad , \tag{13}$$

where $p(n)$ is a parameter ranging from zero (unweighted LSQ) to one (fully weighted LSQ) and n =1, 2 or 3, where n=1 refers to the parameter used for the WLSQ gradients used in the inviscid flux reconstruction, n=2 refers to the parameter used for the WLSQ gradients used in the construction of the cell face gradients for the viscous flux and n=3

refers to the parameter used for the WLSQ gradients used in the construction of turbulence model source terms. With typically p(1)=0 and p(2,3)=1. The overdetermined WLSQ system defined by Eqs. (11-13), can be solved in various ways. We choose to use QR factorization via the Householder transformation [25], which directly solves the overdetermined system as

$$x = R^{-1}Qb, \tag{14}$$

where Q is the orthonormal matrix and R is the upper triangular matrix generated from $\boldsymbol{A}$ by the QR factorization. The solution can then be expressed in the following form:

$$\overline{\nabla q_j} = \begin{bmatrix} \overline{q_j} \\ \overline{\partial_x q_j} \\ \overline{\partial_y q_j} \\ \overline{\partial_z q_j} \end{bmatrix} = \sum_{l \in \{g_l\}} \begin{bmatrix} c^q_{jl} \\ c^x_{jl} \\ c^y_{jl} \\ c^z_{jl} \end{bmatrix} q_l \ , \tag{15}$$

where c^q_{jl}, c^x_{jl}, c^y_{jl} and c^z_{jl} are the WLSQ coefficients to be computed and stored at all nodes once for a given stationary grid. From Eq. (15), it is clear that the cost of the gradient calculation is directly proportional to the number of neighbors involved in the node WLSQ stencil. Furthermore, since we choose to not use the solution value at the node we only need to store the coefficients for the gradient, such that:

$$\overline{\nabla q_j} = \begin{bmatrix} \overline{\partial_x q_j} \\ \overline{\partial_y q_j} \\ \overline{\partial_z q_j} \end{bmatrix} = \sum_{l \in \{g_l\}} \begin{bmatrix} c^x_{jl} \\ c^y_{jl} \\ c^z_{jl} \end{bmatrix} q_l \ . \tag{16}$$

As previously mentioned, there are 2 approaches that use nodal gradients to compute the gradients needed to compute the cell face fluxes. These are the C-ANG approach of Zhang [13-15], which he refers to as a vertex-weighted least-squares (VWLSQ(n)) approach where n is the least-squares weight coefficient and the F-ANG approach of Nishikawa [3].

In the C-ANG approach, the inviscid and viscous cell nodal averaged gradients, $\overline{\nabla q_{ik}}$ and $\overline{\nabla q_{vk}}$, respectively are constructed as the arithmetic average of the nodal gradients from the nodes that define the cell with

$$\overline{\nabla q_{ik}} = [\sum_{j=1}^{N^{nodes}_{cell(k)}} \overline{\nabla q_{ij}}\ ] / N^{nodes}_{cell(k)} \ , \tag{17}$$

$$\overline{\nabla q_{vk}} = [\sum_{j=1}^{N^{nodes}_{cell(k)}} \overline{\nabla q_{vj}}\ ] / N^{nodes}_{cell(k)} \ , \tag{18}$$

where $N^{nodes}_{cell(k)}$ is 3 or 4 in 2-D for triangles or quadrilaterals cells, respectively, and 4, 5, 6 or 8 in 3-D for tetrahedral, pyramidal, prismatic or hexahedral cells, respectively. These cell average gradients are then used to define the inviscid and viscous left and right gradients, $\overline{\nabla q_i^L}, \overline{\nabla q_v^L}, \overline{\nabla q_i^R}$, and $\overline{\nabla q_v^R}$ that appear in Eqs. (1-9) to compute the inviscid and viscous fluxes where

$$\overline{\nabla q_i^L} = \overline{\nabla q_{ik_L}} \text{ and } \overline{\nabla q_i^R} = \overline{\nabla q_{ik_R}} \tag{19}$$

$$\overline{\nabla q_v^L} = \overline{\nabla q_{vk_L}} \text{ and } \overline{\nabla q_v^R} = \overline{\nabla q_{vk_R}} \tag{20}$$

where $\overline{\nabla q_{ik_L}}, \overline{\nabla q_{ik_R}}$ and $\overline{\nabla q_{vk_L}}, \overline{\nabla q_{vk_R}}$ are the left and right, inviscid and viscous, C-ANG WLSQ gradients respectively, defined by Eqs. (16,17,18).

In the F-ANG approach, the inviscid and viscous face nodal averaged gradients, $\overline{\nabla q_{if}}$ and $\overline{\nabla q_{vf}}$, respectively, are computed as the arithmetic average of the nodal gradients from the nodes that define the cell face with

$$\overline{\nabla q_{if}} = [\sum_{j=1}^{N^{nodes}_{face(m)}} \overline{\nabla q_{ij}}\ ] / N^{nodes}_{face(m)} \ , \tag{21}$$

$$\overline{\nabla q_{vf}} = [\sum_{j=1}^{N^{nodes}_{face(m)}} \overline{\nabla q_{vj}}\ ] / N^{nodes}_{face(m)} \ , \tag{22}$$

where $N^{nodes}_{face(m)}$ is the number of nodes that define a face, m, which is 2 in 2-D, and 3 or 4 in 3-D for triangular and quadrilateral faces, respectively. These face averaged gradients, are then used to define the left and right. inviscid and viscous gradients, $\overline{\nabla q_i^L}, \overline{\nabla q_i^R}$ and $\overline{\nabla q_v^L}, \overline{\nabla q_v^R}$ that appear in Eqs. (1-9). As was noted in Refs. [2,3] the F-ANG approach results in the following condition with respect to the left and right inviscid and viscous gradients

$$\overline{\nabla q_i^L} = \overline{\nabla q_i^R} = \overline{\nabla q_{if}} \ , \tag{23}$$

$$\overline{\nabla q_v^L} = \overline{\nabla q_v^R} = \overline{\nabla q_{vf}} \ . \tag{24}$$

There are three reasons that the average nodal gradient approach is potentially superior to the conventional cell-average gradient method. First, the number of nodes is typically smaller than the number of cells in unstructured grids, especially in 3-D on tetrahedral grids, where it is 5-6 times smaller, thus requiring less storage for the gradients (if one chooses to store them). Moreover, if the nodal gradients are computed using a least-squares method, as described in Eq. (10-16), using the cells surrounding the node, the number of coefficients that need to be computed and stored can be significantly smaller than that required for the cell-centered least-squares method for cell gradients described in section *D.1*. Second, the face gradient involves fewer cells than the average of cell gradients at a face, which results in a reduction in the size of the residual stencil. Third, since the gradients are computed at the cell nodes there is, depending on how the gradient limiting is performed, potentially no need to communicate gradient information between processors.

D.2.1. Stable Techniques for Using Node-Centered Gradients to Construct the Inviscid Flux.

In the case of the 2-D hybrid grid cell face shown in red in Fig. 1, three approaches for computing the gradients required to compute the cell face inviscid flux are illustrated in Fig. 6 where l_t and l_q denote stencil cells associated with triangular and quadrilateral cells, respectively. The three approaches are: a) the F-ANG approach [3], b) the C-ANG approach [13-15], and c) the hybrid face and cell averaged nodal gradient approach (FAC-ANG) proposed, analyzed and demonstrated in 2-D in Ref. [2]. Figure 6-a shows that F-ANG results in the most compact flux stencil while Fig. 6-b shows that C-ANG results in the least compact stencil. In Ref. [2], it was shown, via Fourier analysis, that inviscid fluxes computed using F-ANG are unstable on quadrilateral grids, implying that computing inviscid fluxes using F-ANG will also be unstable on hybrid grids containing quadrilaterals. However, Zhang has shown in Refs. [13,14] that the C-ANG approach is stable on triangular, quadrilateral, and hybrid grids. Therefore, to obtain 1) a stable inviscid flux and 2) the smallest possible residual stencil on hybrid grids, the FAC-ANG approach was proposed in Ref. [2]. FAC-ANG, as illustrated in Fig. 6-c, uses F-ANG for the triangular cell side face inviscid flux reconstruction and C-ANG for the quadrilateral cell side face inviscid flux reconstruction.

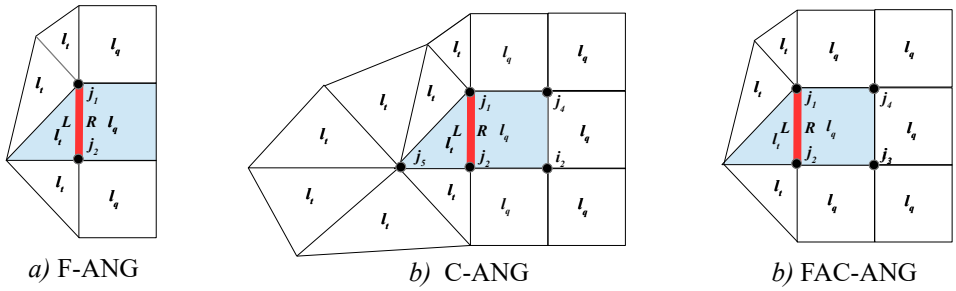

Fig. 6 The 2-D stencils $\{l_i\}$, for computing the WLSQ gradients at the nodes, $j_{1\text{-}N}$, for control volume, k (blue shaded areas), on representative triangular and quadrilateral grids.

The extension of FAC-ANG to 3-D on hybrid grids that may include tetrahedral, pyramidal, prismatic and/or hexahedral cells proceeds as follows: at the cell face, determine if the face is a quadrilateral or a triangle, if the face is a quadrilateral, then construct $\overline{\nabla q}_i^L$ and $\overline{\nabla q}_i^R$ for the cells that share the face, using C-ANG if a cell is a hexahedral and F-ANG if it is not a hexahedral. Or, if the face is a triangle, then construct $\overline{\nabla q}_i^L$ and $\overline{\nabla q}_i^R$ for the cells that share the face, using C-ANG if the cell is a prism and F-ANG if the cell is not a prism. The 3-D extension of the FOC-ANG approach uses the same logic as the FAC-ANG approach and then forces both cells that share the face to use the C-ANG approach if either cell that share the face uses the C-ANG approach.

D.2.2 Stable Techniques for Using Node-Centered Gradients to Construct the Viscous Flux.

In Ref. [2], it was shown that using F-ANG to compute the viscous fluxes is stable independent of the cell topology due to the damping terms in the viscous flux construction Eqs. (6,7). However, it was also shown in Ref. [2] that while using F-ANG to compute $\overline{\nabla q}_v^L$ and $\overline{\nabla q}_v^R$ is stable, using a consistent approach to compute the gradients for the inviscid and viscous fluxes resulted in the best convergence behavior. This observation, obtained in a 2-D code, has not been observed in the 3-D implementation in the VULCAN-CFD code. In 3-D, using the F-ANG approach to compute $\overline{\nabla q}_v^L$ and $\overline{\nabla q}_v^R$, independent of cell topology and how $\overline{\nabla q}_i^L$ and $\overline{\nabla q}_i^R$ are computed, has been observed to be the more robust approach. Moreover, as will be shown in section III, when test case B, which uses a 2-D grid, is run in the 3-D code very little difference in convergence behavior between using F-ANG and FAC-ANG to compute the gradients was observed. The reason for this difference in behavior between the 2-D code and the 3-D code is currently a subject of additional research. One possible explanation is that the difference in behavior is not due to 2-D versus 3-D but is due to the choice of test problems that have been run in the 2-D and 3-D codes. The 2-D test problems run to date have been calorically perfect canonical inviscid and viscous laminar flows to establish the stability and accuracy of the numerical approach, Whereas, the problems run in the 3-D code are calorically-imperfect and/or thermally-imperfect 2-D and 3-D hypersonic turbulent flows that contain strong shocks that interact with the boundary layers and other viscous flow features. Figure 7 illustrates the number of cells and nodes involved in the construction of the viscous flux

contributions to the residual of a quadrilateral cell on a uniformly spaced quadrilateral grid. Figure 7-a shows that the residual stencil that results from using the C-ANG approach to average the node-centered gradients to the cells that share a face with the blue control volume results in a significantly bigger stencil than when the F-ANG approach, shown in Fig. 7-b, is used to average the the node-centered gradients to the faces of the blue control volume. The resulting "compact" nature of the viscous residual stencil produced by the F-ANG approach may have a stabilizing effect when there are strong shocks present.

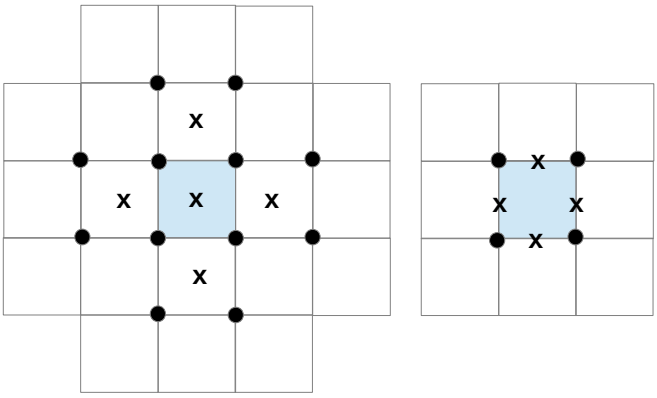

a) C-ANG (21 cells) *b)* F-ANG (9 cells)

Fig. 7 The cells used to compute the viscous flux contribution to the residual of a quadrilateral control volume (blue shaded area), on a quadrilateral grid, where the C-ANG or F-ANG approaches are used to average the nodal (•) WLSQ gradients, to the locations (x), that are used to compute cell face viscous flux gradients, $\overline{\nabla q}_{vf}$.

D.3. Construction of Gradients for Turbulence Transport Equation Source Terms.

The turbulence transport equation source terms require the computation of cell-average gradients of the viscous variables. In the current work, these gradients are formed using Eq. (18) to compute the cell average gradient from the WLSQ node-centered gradients of the viscous primitive variables that were computed for the viscous fluxes. These node-centered gradients are only needed for the cells in the interior of the computational domain eliminating the need to communicate them between processors when computing using a parallel processing paradigm. On a quadrilateral grid, this results in a stencil for the source term gradients that involves nine cells that looks like Fig. 7-b.

E. Inviscid Flux Cell-Average Gradient Limiter Construction.

Being primarily interested in the computation of hypersonic flows containing strong discontinuities, gradient limiters are crucial to the development of a robust numerical scheme. Therefore, the current gradient limiter approach is based on the modified version of *MLP* approach of Park and Kim [26] extensively described in Refs. [4-7]. The *MLP* gradient limiter stencil for reconstruction at a cell face on a mixed-element grid, when using node-centered gradients, is illustrated in Fig. 8. Where the limited reconstructed left and right states can be obtained using Fromm's scheme

$$q^L_{if} = q_{ik_L} + \Phi^{MLP}_{k_L} \overline{\nabla q}^L_i \cdot \vec{r}_{Lf} \tag{25}$$

$$q^R_{if} = q_{ik_R} + \Phi^{MLP}_{k_R} \overline{\nabla q}^R_i \cdot \vec{r}_{Rf} \quad , \tag{26}$$

or the UMUSCL scheme as

$$q^L_{if} = q_{ik_L} + \Phi^{MLP}_{k_L} \{ \Phi^{MLP}_{k_L} \frac{\chi}{2} (q_{ik_R} - q_{ik_L}) + (1-\chi)(\overline{\nabla q}^L_i \cdot \vec{r}_{Lf}) \} \tag{27}$$

$$q^R_{if} = q_{ik_R} + \Phi^{MLP}_{k_R} \{ \Phi^{MLP}_{k_R} \frac{\chi}{2} (q_{ik_L} - q_{ik_R}) + (1-\chi)(\overline{\nabla q}^R_i \cdot \vec{r}_{Rf}) \} \tag{28}$$

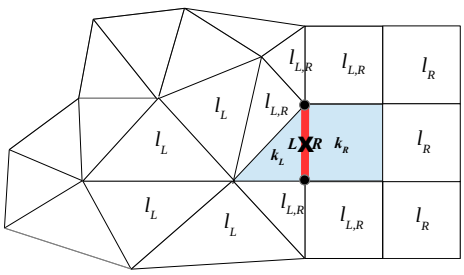

Fig. 8 Left, l_L, and right, l_R, cells participating in the computation of the *MLP* limiter coefficients, $\Phi^{MLP}_{k_L}$ and $\Phi^{MLP}_{k_R}$, respectively, when reconstructing q^L_{if} and q^R_{if}. at the red cell interface when an averaged nodal gradient approach is used to form $\overline{\nabla q}^L_i$ and $\overline{\nabla q}^R_i$.

where $\Phi_{k_L}^{MLP}$ and $\Phi_{k_R}^{MLP}$ are *MLP* gradient limiter coefficients of the left and right cells, respectively, when the C-ANG, FOC-ANG, FAC-ANG or F-ANG approach is used to form $\overline{\nabla q_i}^L$ or $\overline{\nabla q_i}^R$. This approach is based on extensive numerical experimentation and it should be noted that this is the same stencil as when the NN-CCG approach is used to form $\overline{\nabla q_i}^L$ or $\overline{\nabla q_i}^R$.

III. Numerical Results and Discussion

Three canonical 2-D hypersonic flows and one 3-D scramjet inlet flow were computed to demonstrate the numerical behavior of the extension of the 2-D FAC-ANG approach of Ref. [2] to 3-D and compare it with the conventional NN-CCG approach. To the best of our knowledge, the 3-D F-ANG approach is a novel approach, therefore we begin with a numerical experiment where we investigate it's numerical characteristics on a pure tetrahedral grid. This is followed by a second canonical flow on a grid designed to test the behavior of the FAC-ANG and FOC-ANG approaches for a 2-D flow using a 2-D hybrid grid. We then compute a third canonical flow designed to test the behavior of the FAC-ANG and FOC-ANG approaches for a 2-D flow and using 3-D hybrid grid. Finally, the University of Queensland experimental investigation of a 75% scale replica of the HIFiRE 7 REST scramjet engine conducted in the T4 Stalker Tube [27] is simulated using the FAC-ANG, FOC-ANG and NN-CCG approaches and the results are compared with the experimental data. All computations were performed using a 2nd-order cell-centered finite-volume solver [4] implemented in the VULCAN-CFD code. The upwind shock capturing scheme is based on inviscid fluxes computed using either the LDFSS [17] or HLLC [18] approximate Riemann solvers where the higher-order cell-face states are reconstructed using Fromm's method and the cell/face gradients are limited using a modified version [4,6] of the *MLP-u2* limiter of Park and Kim [26]. The viscous fluxes are computed using the alpha damped cell-face gradient method of Nishikawa [24] except for the HIFiRE 7 case, which uses the face tangent method of Hasselbacher [21]. The governing equations were solved implicitly combining local time stepping using the parallel implementation of a Symmetric Gauss-Seidel (SGS) scheme described in Ref. [4] using 1st-order inviscid and thin layer viscous flux Jacobians. For each computation, stencil statistics and cost, contour plots of the flow solution, wall heat flux distribution and convergence behavior were extracted and are presented.

A . Hypersonic Turbulent Flow Over a 2-D Flat Plate Using a Grid Only Containing Tetrahedral Cells.

The first numerical experiment was chosen to investigate the numerical behavior of the 3-D extension and implementation of F-ANG on a pure tetrahedral grid using a canonical 2-D hypersonic turbulent boundary layer flow. This numerical experiment was conducted by computing thermally-prefect, chemically-frozen, turbulent flow of air over a 2-D flat plate with freestream conditions of Mach number, M_{ref}=6.0, static pressure, P_{ref}= 2100.0 Pascals, static temperature, T_{ref}= 63.01 Kelvin, and unit Reynolds number, Re_{ref}= 2.64x107/m, with the wall treated as an isothermal (335.83 Kelvin), no-slip, solve-to-the-wall boundary condition. The Wilcox (1998) $k-\omega$ two-equation turbulence model [30] was used to compute the Reynolds stresses and Reynolds heat flux (Pr_t=0.9), and the turbulence model production term was based on the magnitude of the vorticity. The 2-D geometry was discretized to form a 3-D computational domain using the Pointwise® unstructured grid generator. The resulting grid consisted of triangles on the surface of the plate and a 3-D grid of 582,605 tetrahedral cells as shown in Fig. 9. The boundary conditions were: 1) reflection of all variables at the min. and max. Z-direction boundary cell faces, 2) specification of all variables on the min. X-direction boundary cell faces, 3) 1st-order extrapolation of all variables at the max. X- and Y-direction boundary cell faces and 4) a no-slip, isothermal, solve-to-the-wall BC on the min. Y-direction wall boundary cell faces. The computational domain was decomposed into 24 partitions. The governing equations were solved implicitly, in a fully coupled manner, using local time stepping, and the global CFL number was linearly varied from 0.1 to 250 over iterations 1 to 500. The FAC-ANG approach was used, which recovers the F-ANG approach for tetrahedral cells, to compute the gradients on this 3-D tetrahedral grid. Computations were performed using the NN-CCG and F-ANG approaches with all other input parameters remaining unchanged.

Table 1 presents the stencil statistics of the NN-CCG and node-centered gradient (NCG) approaches. In addition, the cost and relative cost of computing the WLSQ gradients, where the cost is defined as the number of WLSQ locations (the number of cells for the cell-centered gradient and the number of nodes for the node-centered gradient approaches, respectively), times the mean stencil size. These figures of merit indicate that the node-centered gradient approach produced stencils that were smaller in the mean as well as having a much smaller standard deviation. Table 1 also reveals that the F-ANG approach required approximately 14 times less storage and operations to compute the gradients than the NN-CCG approach.

Table 1 Stencil statistics and cost of the gradient approaches used to compute the 2-D flat plate.

WLSQ Gradient Approach	Number of WLSQ Stencils	Minimum Stencil Size	Mean Stencil Size	Maximum Stencil Size	Stencil Size Standard Deviation	WLSQ Cost (No. of Stencils x Mean Stencil Size)	WLSQ Relative Cost
NN-CCG	582,605 (cells)	4	66.1	106	11.2	38510191	1.0
NCG (F-ANG)	116,469 (nodes)	6	23.3	46	1.91	2713728	1.0 / 14.2

Figure 10 presents a comparison of Mach number and static pressure contours. The flow solution can be seen to be nearly oscillation free with the weak leading edge shock caused by the rapid growth in the displacement thickness during the initial boundary layer formation with the weak leading edge shock being captured with only minor differences. Figure 11 presents a comparison of the axial distribution of the wall heat flux. The heat flux computed using the F-ANG approach is shown to be significantly less noisy than the heat flux computed using the NN-CCG approach. This result is very encouraging since, as was stated in the introduction, we are interested in gradient methods that work better than the current state-of-the-art on tetrahedral grids due to our interest in tetrahedral-based unstructured-grid adaptation. Figure 12 presents a comparison of the convergence history of the reduction of the L_2 norm of the residual showing that both gradient approaches produced essentially identical convergence behavior.

B. Hypersonic Turbulent Flow Over a 2-D Backward Facing Step Using a Grid Containing Prismatic and Hexahedral Cells.

The second numerical experiment was chosen to investigate the numerical behavior of the 3-D extension and implementation of FAC-ANG, and the alternative approach, FOC-ANG, on a 2-D grid containing hexahedral and prismatic cells. This flow was chosen because it contains a multiplicity of hypersonic flow phenomenon, 1) turbulent boundary layers, 2) a strong expansion, 3) a turbulent free shear layer, and 4) a shock-turbulent-boundary-layer interaction. This numerical experiment was conducted by computing the hypersonic calorically perfect, chemically-frozen, turbulent flow of air over a 2-D backward facing step with freestream conditions of, Mach number, M_{ref}=6.356, static pressure, P_{ref}= 50,662.58 Pascals, static temperature, T_{ref}= 1297.75 Kelvin, ratio of specific heats, $gamma_{ref}$= 1.4, and unit Reynolds number, Re_{ref}= 1.2891×10^7/m, with the no-slip wall treated as isothermal (1172.6 Kelvin), using a turbulent wall matching boundary condition [28]. The Wilcox (2006) $k-\omega$ two-equation turbulence model [29] was used to compute the Reynolds stresses and Reynolds heat flux (Pr_t=0.9) and the turbulence model production term was based on the magnitude of the vorticity. The 2-D geometry was discretized to form a 3-D computational domain using the Pointwise® unstructured grid generator. The resulting grid consisted of triangular and quadrilateral 2-D cells, as shown in Fig. 13, extruded in the Z-direction to form a 3-D grid of 15,781 prismatic and 8,168 hexahedral cells for a total of 23,949 cells. The boundary conditions were: 1) reflection of all variables at the min. and max. Z-direction boundary cell faces, 2) specification of all variables on the min. X-direction boundary cell faces, 3) 1st-order extrapolation of all variables at the max. X- and Y-direction boundary cell faces and 4) isothermal no-slip wall-matching construction of all variables on the min. Y-direction wall boundary cell faces. The computational domain was decomposed into 6 partitions. The governing equations were solved implicitly, in a fully coupled manner, using local time stepping, and the global CFL number was linearly varied from 0.1 to 250 over iterations 1 to 500.

Table 2 presents the stencil statistics of the NN-CCG and node-centered gradient (NCG) FAC-ANG and FOC-ANG approaches. These figures of merit show that the node-centered gradient approach produced stencils that were smaller in the mean as well as having a lower standard deviation. Table 2 also reveals that the NCG approaches required approximately 2.4 times less storage and operations to compute the gradients than the NN-CCG approach.

Table 2 Stencil statistics and cost of the gradient approaches used to compute the 2-D backward facing step.

WLSQ Gradient Approach	Number of WLSQ Stencils	Minimum Stencil Size	Mean Stencil Size	Maximum Stencil Size	Stencil Size Standard Deviation	WLSQ Cost = (No. of Stencils x Mean Stencil Size)	WLSQ Relative Cost
NN-CCG	23,949 (cells)	13	33.8	53	6.2	809476	1.0
NCG	32,762 (nodes)	6	10.1	18	2.5	330896	1.0 / 2.4

Figure 14 presents a comparison of contour plots of Mach no. (filled) contours and the static pressure (black lines) contours using the NN-CCG and FAC-ANG approaches. The FOC-ANG approach is not shown because its solution was essentially identical to the FAC-ANG solution. Both flow solutions are very similar and can be seen to be nearly oscillation-free with the incident shock caused by the reattachment of the separation bubble being captured without apparent difficulty. Figure 15 presents a comparison of the axial distribution of the wall heat flux. The heat flux computed using all three approaches are nearly identical and do not contain the oscillations that were observed in the tetrahedral-grid-based flat plate results. Figure 16 presents a comparison of the convergence behavior of the NN-CCG, FAC-ANG and FOC-ANG approaches, showing that the averaged nodal gradient (ANG) approaches gave nearly identical convergence behavior and that the NN-CCG approach convergence was slightly better. This result is consistent with the 2-D convergence behavior observed in Ref. [2].

C. Hypersonic 2-D Turbulent Flow Over a 2-D Blunt Wedge Using a Grid Containing Tetrahedral, Pyramidal, Prismatic and Hexahedral Cells.

The third numerical experiment was chosen to test the behavior of the FAC-ANG and FOC-ANG approaches using a 2-D flow and a 3-D hybrid grid containing tetrahedral, prismatic, pyramidal and hexahedral cells. This flow was chosen because it contains a strong Mach 8 blunt body normal shock that is a good test of the robustness of the shock capturing scheme. This tests the implementation of the node-centered gradients on all element types allowed by the code thus testing the behavior of the FAC-ANG and FOC-ANG approaches for hexahedrals that share faces with both

pyramidal and prismatic cells. This numerical experiment was conducted by computing hypersonic, thermally-prefect, chemically-frozen, turbulent flow over a blunt wedge representing a scramjet forebody or cowl leading edge (this particular geometry uses the same diameter blunt body as the REST inlet cowl [27]). The freestream conditions were: P_{ref}= 1675.0 Pascals, T_{ref}= 226.7 Kelvin, and Mach number, M_{ref}= 8.0. A thermally-perfect air gas mixture was used to simulate the test gas, which, at the given conditions, yields a unit Reynolds number of Re_{ref}= 2.9467x10^6/m. The wall surface was treated as a no-slip, isothermal (300.0 Kelvin) wall, using a turbulent wall matching boundary condition [28]. The Menter Baseline two-equation turbulence model [31] was used to compute the Reynolds stresses and Reynolds heat flux (Pr_t=0.9), and the turbulence model production term was based on the magnitude of the vorticity. Convergence was achieved by "freezing" the gradient limiter after 1500 time steps to prevent convergence stalling due to limiter "ringing". The blunt wedge geometry was discretized to form a 3-D computational domain using the Pointwise® unstructured grid generator. The resulting grid consisted of quadrilaterals on the surface of the wedge that were extruded normal to the surface to form layers of hexahedral cells in the near wall, which were transitioned to tetrahedral cells via a layer of pryamidal cells to form a 3-D grid of 364,380 hexahedral, 14,840 prismatic, 67,519 pyramidal and 647,424 tetrahedral cells for a total of 1,094,163 cells presented in Figs. 17 and 18. The boundary conditions were: 1) reflection of all variables at the min. and max. Y-direction boundary cell faces, 2) specification of all variables on the parabolic-shaped freestream surface boundary cell faces, 3) 1st-order extrapolation of all variables at the max. X-direction boundary cell faces and 4) isothermal wall-matching on the wall boundary cell faces. The computational domain was decomposed into 24 partitions. The governing equations were solved implicitly, in a fully coupled manner, using local time stepping, and the global CFL number was linearly varied from 0.1 to 50 and 50 to 250 over iterations 1 to 50 and 50 to 1000, respectively. The gradient limiter was frozen at iteration number 1,500 to eliminate limiter buzz that began to appear near iteration 600.

Table 3 presents the stencil statistics of the NN-CCG and node-centered gradient (NCG) FAC-ANG and FOC-ANG approaches. These figures of merit show that the node-centered gradient approach produced stencils that were significantly smaller in the mean as well as having a much lower standard deviation. Table 3 also reveals that the NCG approaches required approximately 9.1 times less storage and operations to compute the gradients than the NN-CCG approach.

Table 3 Stencil statistics and cost of the cell and node-centered gradient approaches for the 2-D blunt body grid.

WLSQ Gradient Approach	Number of WLSQ Stencils	Minimum Stencil Size	Mean Stencil Size	Maximum Stencil Size	Stencil Size Standard Deviation	WLSQ Cost = (No. of Stencils x Mean Stencil Size)	WLSQ Relative Cost
NN-CCG	1,094,163 (cells)	4	54.5	133	22.18	59631884	1.0
NCG	522,401 (nodes)	6	12.8	50	4.96	6686733	1.0 / 9.1

Figures 19 and 20 present contour plots of Mach number using the FAC-ANG approach and are typical of the results obtained using all three approaches. Figures 19 and 20 show that the flow solution can be seen to be nearly oscillation free with the bow shock being well captured. Figure 20, which presents a close up of the blunt body bow shock on the cutting plane grid presented in Fig. 18, is carbuncle free and well captured in approximately three cells in the hexahedral cell part of the grid in the vicinity of the stagnation streamline. Figure 21 presents a comparison of the normalized wall heat flux versus normalized arclength showing that all three gradient approaches produced results that are nearly identical. Figure 22 presents a comparison of the convergence history of the reduction of the L_2 norm of the residual for all three gradient approaches, showing that the FAC-ANG and FOC-ANG approaches produced similar convergence behavior until the the limiter was frozen. After the limiter was frozen, the NN-CCG, FAC-ANG and FOC-ANG approaches all gave similar asymptotic convergence behavior. However, it should be noted that the FAC-ANG approach produced a small spike near iteration 1700 that is absent from the FOC-ANG and NN-CCG residual histories. This may be an indication that the FOC-ANG approach may be preferable to the FAC-ANG approach on truly 3-D grids, when there are large numbers of pyramidal and/or prismatic cells that share a face with a hexahedral cell.

D. HIFiRE 7 REST Scramjet Engine Shock Tunnel Data Using a Grid Containing Tetrahedral, Pyramidal, Prismatic, and Hexahedral Cells.

The University of Queensland experimental investigation of a 75% scale replica of the HiFiRE 7 REST scramjet engine conducted in the T4 Stalker Tube [27] has been simulated previously using the unstructured-grid solver [4,7]. An early implementation of the *fn2* stencil was used in Ref. [4] and more efficient stencil based on the Frabenius Norm were used in Ref. [7] and very good comparisons with the inlet centerline experimental data were obtained. In the current work, the unstructured-grid solver was again used to compute the zero degrees angle-of-attack tare (no fuel injection) test point. As previously, the bilateral symmetry of the model geometry was exploited to generate a computational mesh for half of the REST scramjet flow path shown in Fig. 23, using the Pointwise® unstructured grid generator. The resulting surface grid was predominantly made up of triangles with quadrilaterals being used along the blunt leading edges and in the internal portion of the flow path. This surface grid was then marched normal to the wall surface into the interior of the computational domain to form a boundary layer grid made up of prisms and hexes. This

boundary layer grid then transitioned into pyramidal and tetrahedral cells resulting in a mixed cell grid. The resulting grid had a total of 44,568,851 cells consisting of 19,198,513 tetrahedral, 1,436,197 pyramidal, 18,455,646 prismatic, and 5,488,495 hexahedral cells. The grid was decomposed into 768 partitions.

In Ref. [4], the unstructured-grid solver was run with an early implementation of the FN2-CCG stencil, with the same inflow/reference conditions that Chan et al. used in Ref. [27] to perform their CFD simulation using the VULCAN-CFD structured-grid solver. These conditions were: P_{ref}= 1675.0 Pascals, T_{ref}= 228.0 Kelvin, and velocity, U_{ref}= 2379 m/s. As mentioned above, the zero degree angle-of-attack, tare case, was selected. However, it is important to note that the angle-of-attack convention reported in [27] is relative to the combustor centerline. The angle-of-attack relative to the x-axis, which runs parallel to the forebody plate, is 6 degrees, as shown in Fig. 23. A thermally-perfect, chemically-frozen air gas mixture was used to simulate the test gas, which at the given reference conditions yields a Mach number, M_{ref}, of 7.845 and a unit Reynolds number of Re_{ref}= 4.1x10^6/m. The model surfaces were treated as no-slip, isothermal (300.0 Kelvin) walls, using the Wilcox wall matching formulation [28]. The Menter Baseline two-equation turbulence model [31] was used to compute the Reynolds stresses and Reynolds heat flux (Pr_t=0.9). The boundary layer trips were not modeled. The computational domain was initialized to the reference conditions, and a 5-mm thick "initial boundary layer" was constructed by linearly blending the no-slip isothermal wall condition into the interior of the computational domain. The cell face gradients for the viscous fluxes, $\overline{\nabla q}_{v\,f}$ were computed using the face tangent approach of Hasselbacher [21] for the current results to be consistent with the results presented previously [4,7].

A Mach contour plot on the symmetry plane of the forebody and inlet, superimposed over the computational grid, is presented in Fig. 24. All three gradient approaches produced solutions with nearly identical contours and only the FAC-ANG results are shown. Figure 24 illustrates the small size of the forebody and cowl leading edges relative to the forebody boundary layer thickness. In addition, Fig. 24 shows that the shocks are captured without significant oscillations and that the forebody leading edge and forebody compression corner shocks are both captured with a small number of cells even where the grid is predominantly tetrahedral in nature.

Table 4 presents the stencil statistics of the NN-CCG and node-centered gradient (NCG) FAC-ANG and FOC-ANG approaches. These figures of merit show that the node-centered gradient approach produced stencils that were significantly smaller in the mean as well as having a much lower standard deviation. Table 4 also reveals that the NCG approaches required approximately 8.5 times less storage and operations to compute the gradients than the NN-CCG approach.

Table 4 Stencil statistics and cost of the cell and node-centered gradient approaches for the HIFiRE 7 Inlet grid.

WLSQ Gradient Approach	Number of WLSQ Stencils	Minimum Stencil Size	Mean Stencil Size	Maximum Stencil Size	Stencil Size Standard Deviation	WLSQ Cost = (No. of Stencils x Mean Stencil Size)	WLSQ Relative Cost
NN-CCG	44,568,851 (cells)	4	51.8	129	19.1	2,308,666,482	1.0
NCG	18,805,899 (nodes)	5	14.5	141	4.07	272,685,536	1.0 / 8.5

Figure 25 presents a comparison of the convergence history of the reduction of the L_2 norm of the residual for the NN-CCG, FAC-ANG and FOC-ANG computations. The computation was run for 1250 iterations using a 1st-order advection scheme to establish the flow. The advection scheme was then switched to the 2nd-order scheme, and the solution was run an additional 2250 iterations. The gradient limiter was then frozen at iteration 3000, which can be seen in the residual plot in Fig. 25, as an abrupt drop in the residual. The solution was then run for an additional 500 iterations to make certain that each solution was stable with the frozen limiter. It was deemed "safe" to freeze the limiter at cycle 3000 because the mass flow error, surface integrated heat transfer, as well as the integrated forces and moments had all reached an asymptotic value. This approach resulted in the L_2 of the Residual of the NN-CCG, FAC-ANG and FOC-ANG approaches converging approximately at least 6.0 orders of magnitude relative to the maximum value. The convergence of the NN-CCG approach appears to be the best plateauing at a minimum value of 6.4 orders of magnitude lower than the maximum value near iteration 2500 with the limiter freezing having no discernible effect. The nodal-averaged gradient methods are shown to have only converged 5 orders of magnitude at iteration 2500 and they do not reach 6 orders until after the limiter is frozen. This difference in the achieved level of convergence before and after the freezing of the limiter suggests that the limiter is acting more aggressively in the computations using the FAC-ANG and FOC-ANG approaches. Further investigation of this behavior is planned as future work.

The body side and inlet cowl side wall static pressure at the symmetry plane are presented in Figs. 26 and 27 showing that the comparison of the wall pressure distribution with respect to the experimental wall pressure data is very reasonable. Figures 28 and 29 present a comparison of the body and cowl centerline wall heat flux using the four stencils. All three gradient approaches give very similar "global" wall heat transfer distributions, in terms of the location and number of minima and maxima on the body and cowl side. However, on the cowl side, the FAC-ANG and FOC-ANG approaches are essentially identical; there are some small differences between them and the NN-CCG approach at select minima and maxima locations that are highlighted in Fig. 29.

IV. Summary and Conclusions

The development of a novel gradient construction approach was pursued due to a near-term desire to reduce, in terms of computational effort and storage, the cost of computing weighted least-squares gradients (WLSQ) on general unstructured grids. We were further motivated by a long term need to improve the fidelity and robustness of the cell-centered, finite-volume, unstructured grid method on the highly skewed tetrahedral grids that can be produced by current tetrahedral cell unstructured grid adaptation algorithms.

In particular, the 2-D nodal-gradient approach of Zhang, a method for computing WLSQ gradients at the grid nodes, and the related 2-D face-averaged nodal-gradient (F-ANG) approach of Nishikawa and White were described and extended to 3-D. This resulted in the development a novel 3-D approach for the computation of WLSQ gradients at the nodes, the averaging of those nodal gradients to the cell face, and the use of the averaged nodal gradients in constructing the inviscid and viscous fluxes in a 2nd-order accurate, cell-centered, finite-volume unstructured tetrahedral-grid-based solver. The fidelity and robustness of this 3-D F-ANG approach was compared with a conventional, 3-D, node-neighbor cell-centered gradient approach (NN-CCG) through the simulation of turbulent hypersonic flow of thermally-perfect air over a flat plate using a highly stretched tetrahedral grid. For this tetrahedral grid, the 3-D nodal gradient approach was found to reduce the cost of computing the WLSQ gradients by a factor of 14 compared to the 3-D NN-CCG approach. In addition, the 3-D F-ANG approach to constructing the gradients that are required to compute the inviscid and viscous fluxes, was found to dramatically reduce numerical noise/oscillations in the computed axial distribution of wall heat flux compared to the NN-CCG approach. Moreover, the convergence of the F-ANG and NN-CCG approaches, on this high aspect ratio tetrahedral grid, were both found to be well behaved and nearly identical.

In an effort to to make the nodal-gradient-based 3-D F-ANG approach more general, it was extended to include grids that contain nonsimplex cells. This extension was achieved using an approach analogous to that described in the recent paper by Nishikawa and White that developed an extension of the 2-D F-ANG approach to nonsimplex 2-D cells by combining face and cell-averaged nodal gradients (C-ANG) in a cell topology dependent manner that was called FAC-ANG. The 3-D extension of FAC-ANG and an alternative approach, FOC-ANG, were described as was a multidimensional gradient limiter procedure that is consistent with the residual stencil. The nodal WLSQ gradient-based FAC-ANG and FOC-ANG approaches as well as the cell-centered WLSQ gradient NN-CCG approach to computing the gradients were tested and compared. Three numerical test cases involving 2-D and 3-D, noncalorically-perfect, turbulent hypersonic flows, on 2-D and 3-D grids containing hexahedral, prismatic, pyramidal and tetrahedral cells were used to perform these tests. Overall, these numerical tests revealed that the computational cost saving provided by using a nodal WLSQ gradient approach on a grid containing nontetrahedral cells, while not as great as on pure tetrahedral grids, was still between 2.4 and 9 times less than the cost of computing the WLSQ gradients using the NN-CCNG approach. For the 2-D backward facing step and the 2-D blunt wedge numerical tests, the axial distribution of wall heat flux and the convergence of the L_2 norm of the FAC-ANG and the FOC-ANG approaches were found to be nearly identical. For the fully 3-D grid and 3-D hypersonic turbulent flow of the HIFiRE 7 REST scramjet inlet, the computed wall pressures of all three approaches were in very good agreement with the experimental data. Moreover, the computed body side and cowl side centerline axial wall heat flux distributions of the three approaches were very similar with only small differences existing on the cowl side. However, the convergence of the FAC-ANG and FOC-ANG approaches while nearly identical to each other, were not quite as good as the NN-CCG approach. Additional analysis of the HIFiRE 7 REST scramjet inlet results is ongoing.

In summary, the FAC-ANG and FOC-ANG approaches, which recover the F-ANG approach on tetrahedral cells, have proven to be robust and to converge relatively well. Furthermore, the FAC-ANG and FOC-ANG approaches have also been shown to: 1) produce wall heat flux results that are superior to the NN-CCG approach on a grid with tetrahedral wall cells and as good as the NN-CCG approach on multiple grids containing hexahedral and/or prismatic wall cells, 2) have WLSQ stencils that were 3 to 4 times smaller, in the mean, than the NN-CCG approach, and 3) have a WLSQ gradient computational cost 2.4 to 14 times less than the NN-CCG WLSQ cost. Therefore, two of the three potential advantages of the averaged nodal gradient approach discussed in the introduction have been substantiated. However, the third potential advantage, reducing the amount of interpartition communication, could not be realized due to the need to communicate gradients because of gradient limiters for all grid cell types and on hybrid grids where the C-ANG approach requires data from nodes that reside on other partitions.

Acknowledgments

This work was supported by the Hypersonic Technology Project, through the Hypersonic Airbreathing Propulsion Branch of the NASA Langley Research Center. In addition, we would like to thank Dr. Boris Diskin, of the National Institute of Aerospace, for his many helpful suggestions and Dr. Michael Smart, of the University of Queensland for providing the HIFiRE geometry.

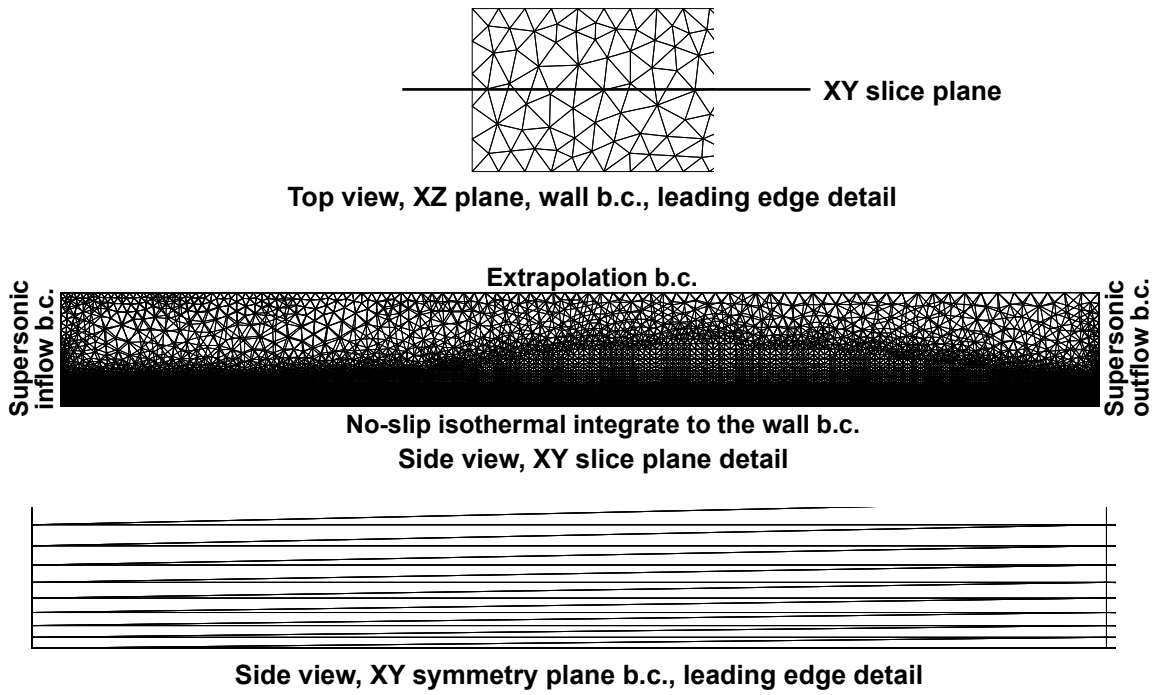

Fig 9 Mach 6 , 2-D, turbulent flat plate, 3-D tetrahedral cell grid details.

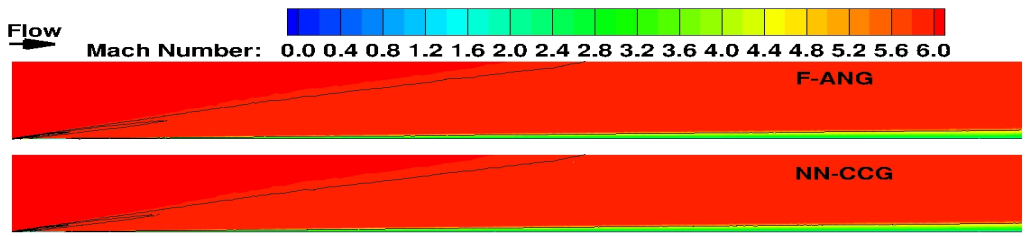

Fig. 10 Mach 6, 2-D, turbulent flat plate, tetrahedral grid, comparison of F-ANG and NN-CCG solutions using Mach number (color filled contours) and static pressure (black contour lines).

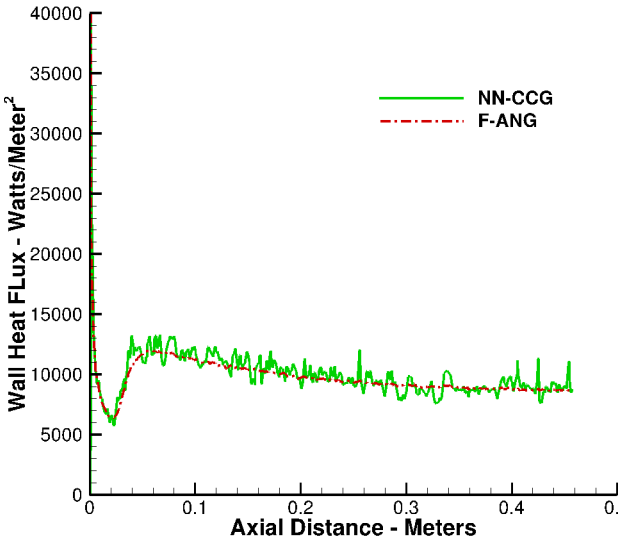

Fig. 11 Mach 6, 2-D, turbulent flat plate, computed wall heat flux.

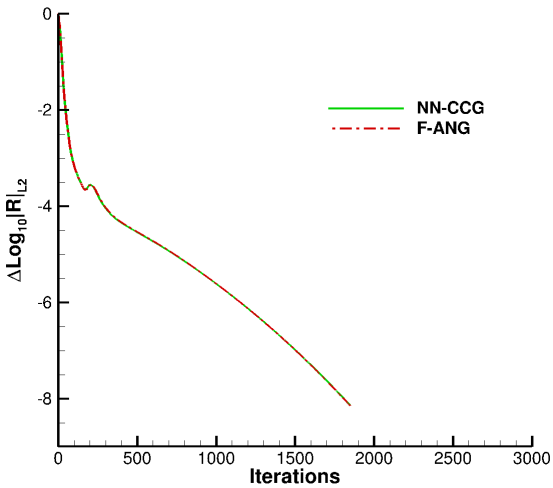

Fig. 12 Mach 6, 2-D, turbulent flat plate, convergence behavior.

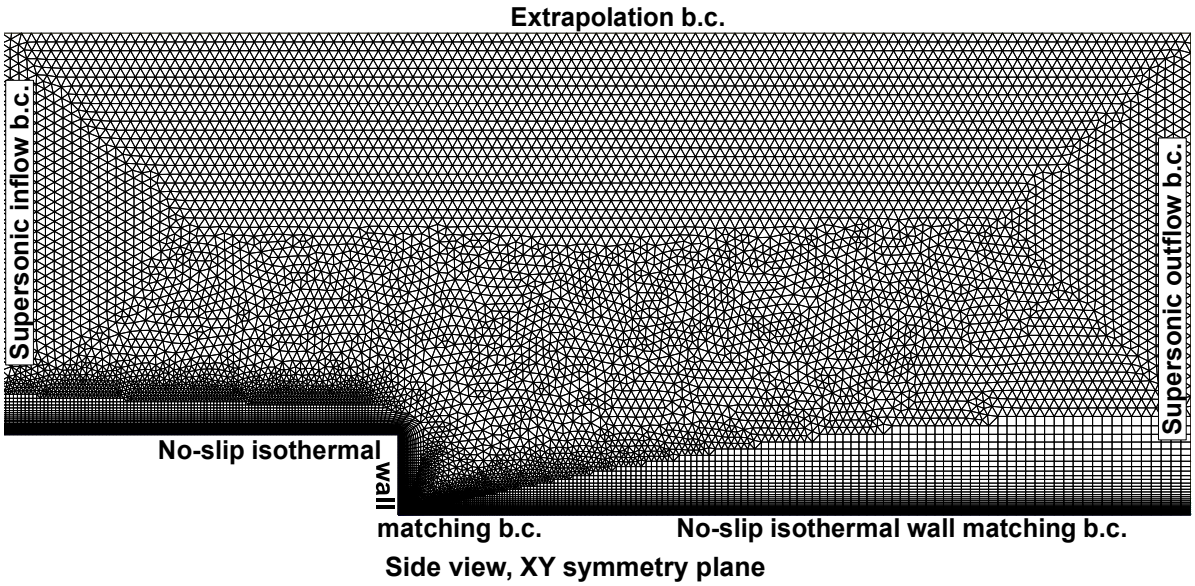

Fig. 13 Mach 6.4 , 2-D, turbulent backward facing step, 2-D hexahedral and prismatic cell grid details.

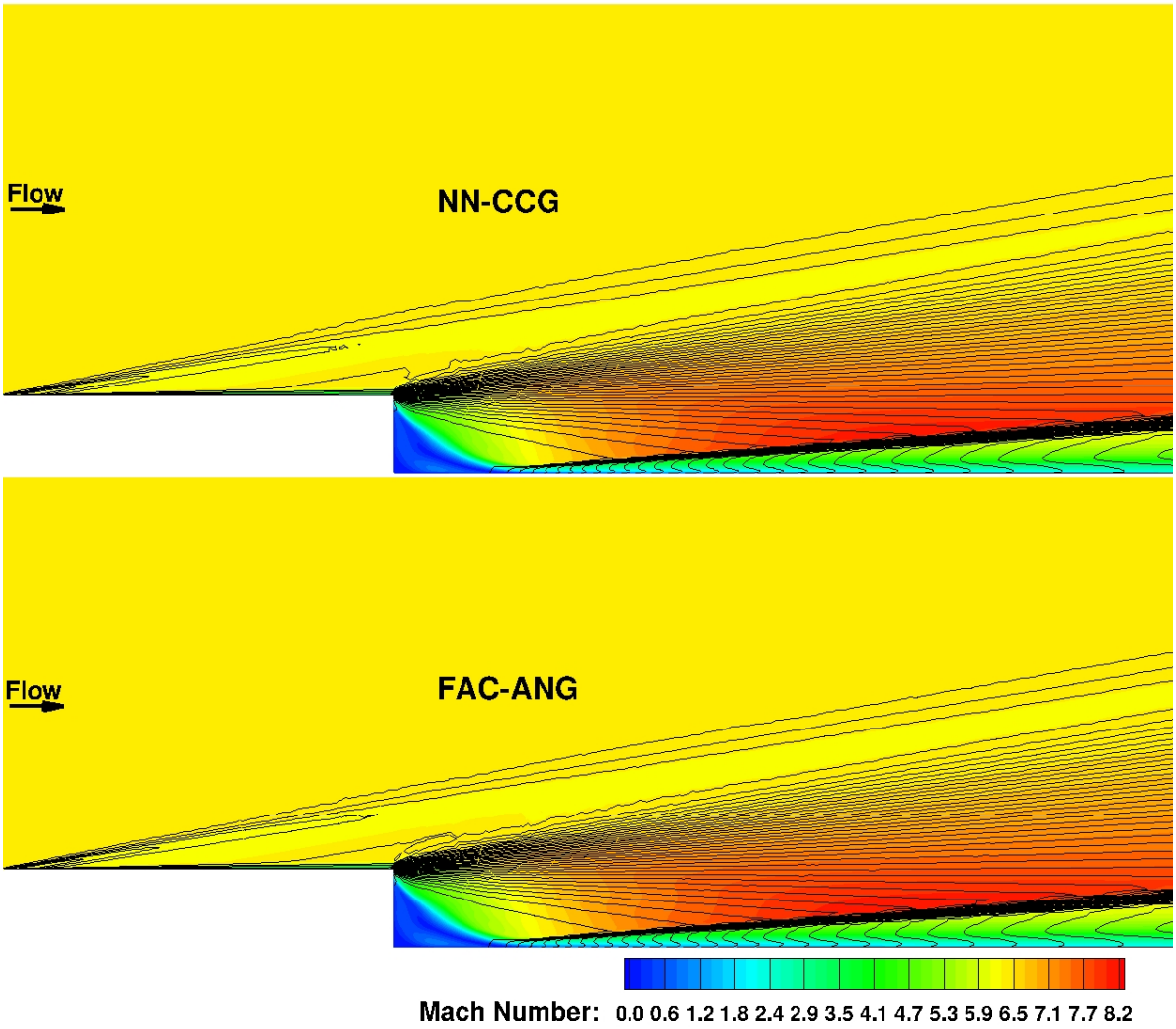

Fig. 14 Mach 6.4, 2-D, turbulent backward facing step, 2-D hexahedral and prismatic cell grid, comparison of F-ANG and NN-CCG solutions using Mach number (color filled contours) and static pressure (black contour lines).

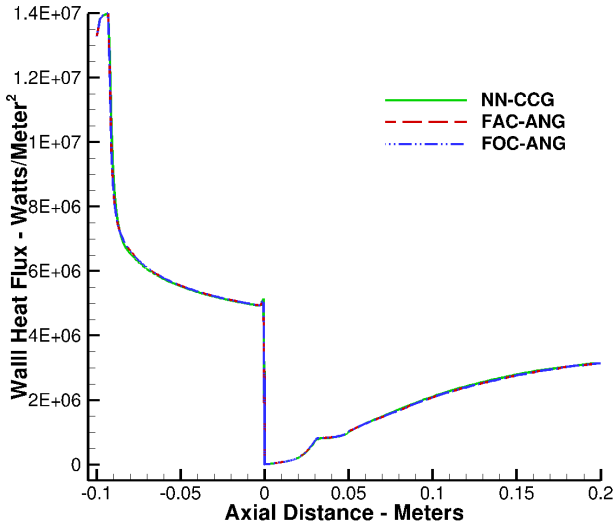

Fig. 15 Mach 6.4, 2-D, turbulent backward, facing step, computed wall heat flux.

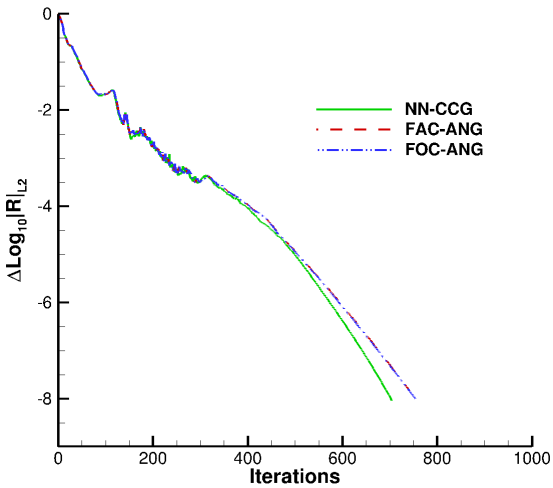

Fig. 16 Mach 6-4, 2-D, turbulent backward, facing step, convergence behavior.

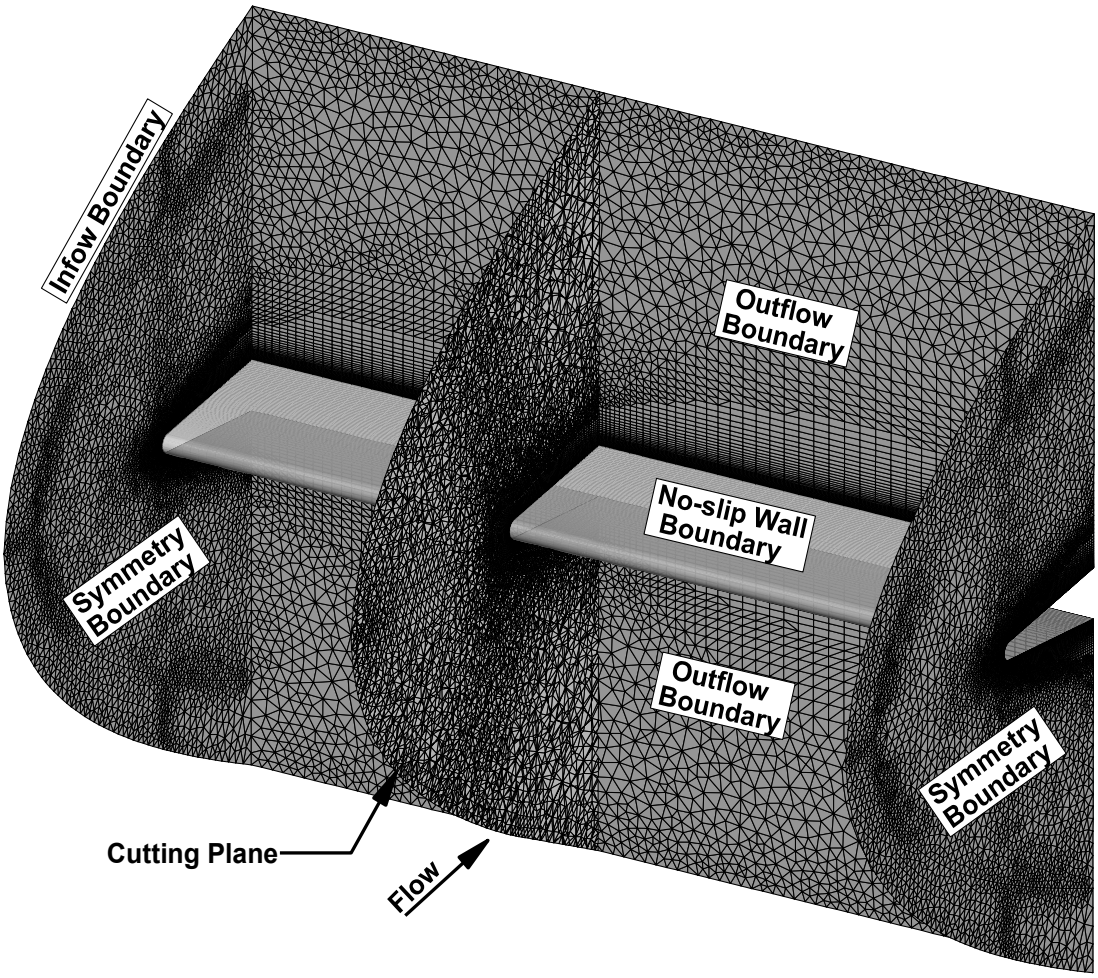

Fig 17 Mach 8.0, 2-D turbulent blunt wedge, 3-D hexahedral, pyramidal, prismatic and tetrahedral cell grid details.

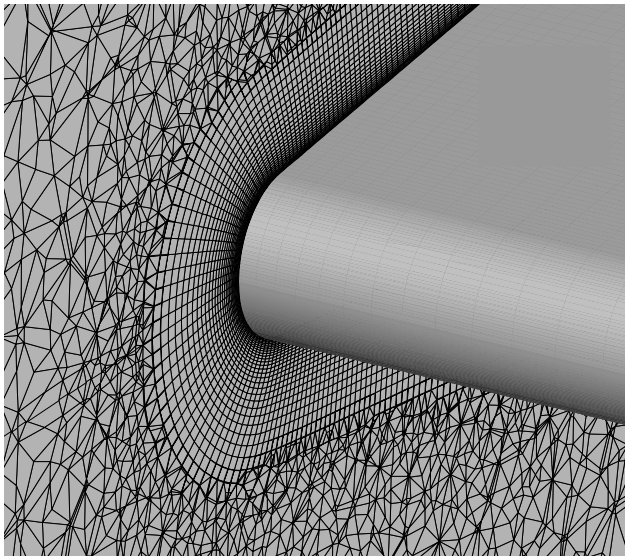

Fig. 18 Mach 8.0, 2-D turbulent blunt wedge, 3-D hexahedral, pyramidal, prismatic and tetrahedral cell grid leading edge cutting plane grid details.

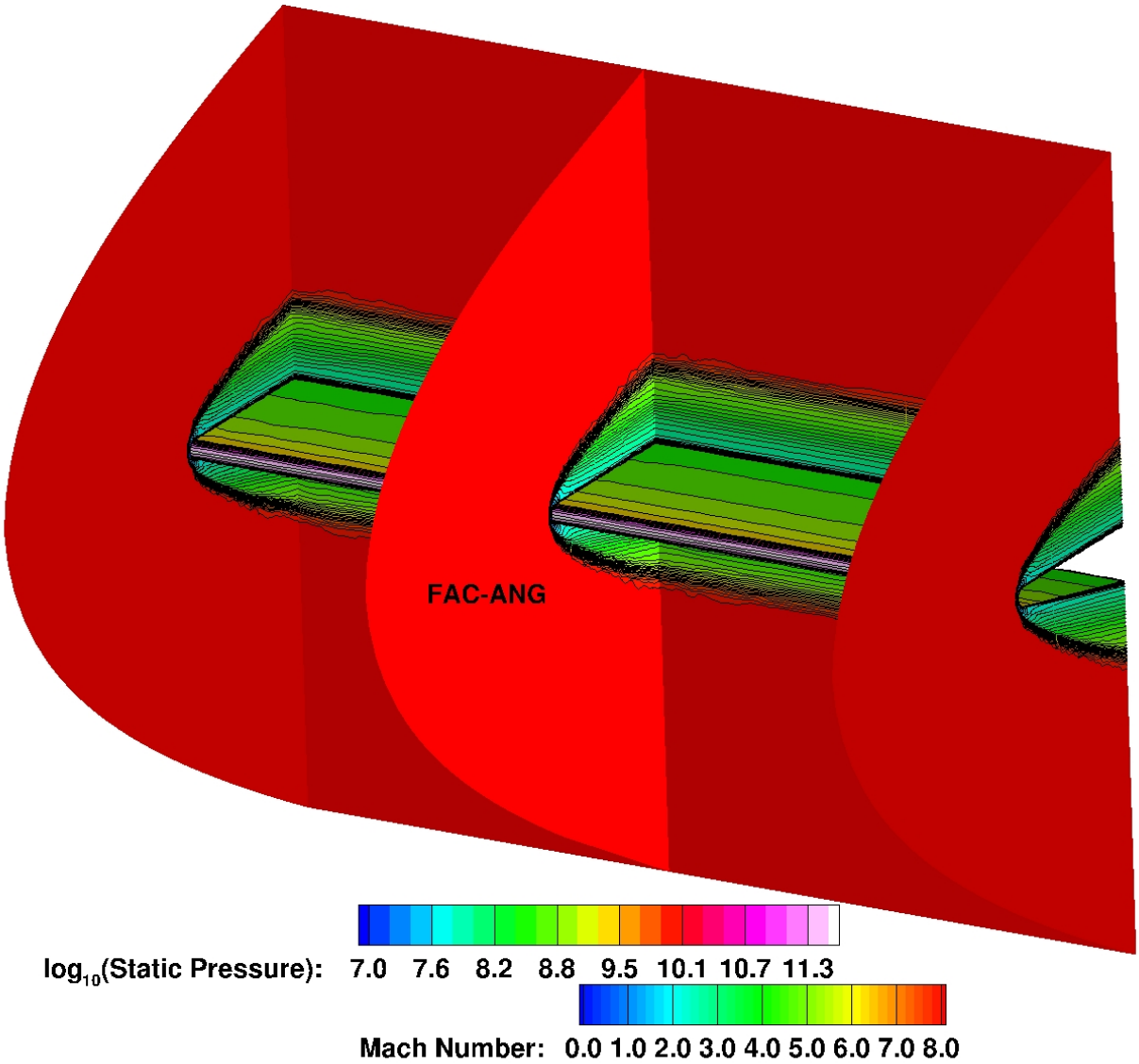

Fig. 19 Mach 8.0, 2-D turbulent blunt wedge flow solution using the FAC-ANG approach, view showing Mach contours on the symmetry, outflow and cutting planes, and $\log_{10}$(Static Pressure) contours on the no-slip wall surface.

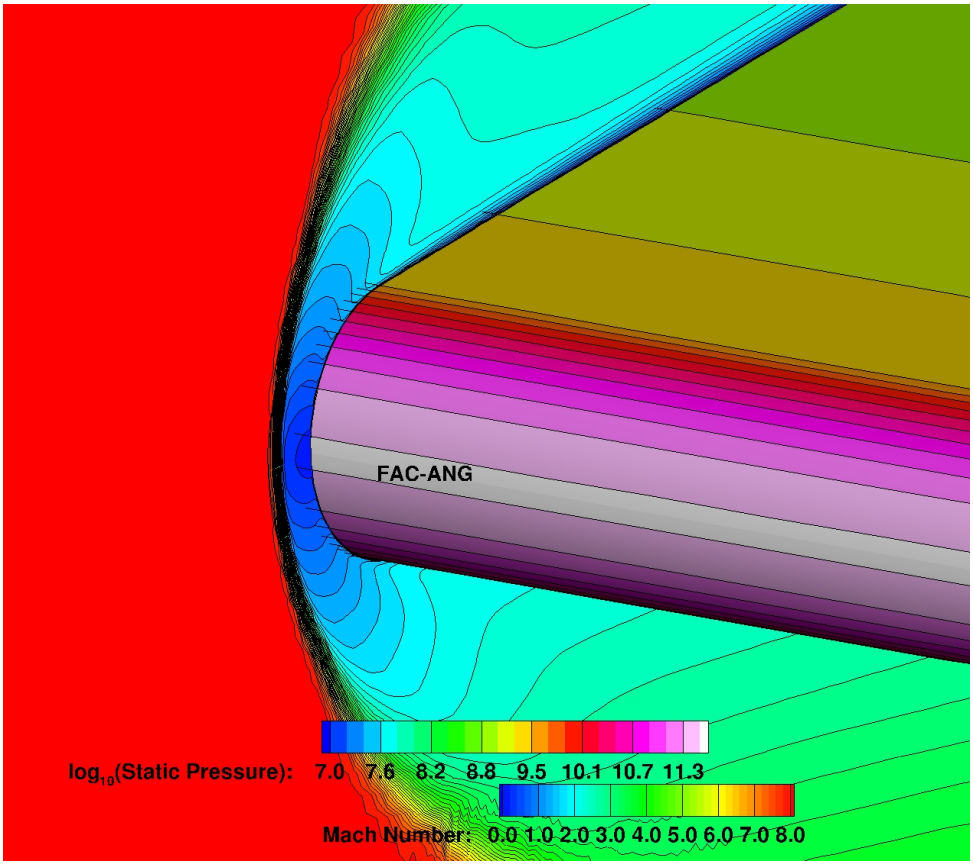

Fig. 20 Mach 8.0, 2-D turbulent blunt wedge flow solution using the FAC-ANG approach, detail view near the leading edge showing Mach contours on the cutting plane and $\log_{10}$(Static Pressure) contours on the no-slip wall surface.

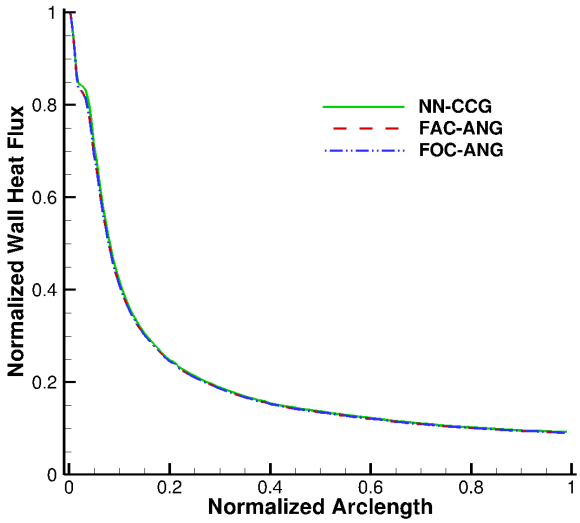

Fig. 21 Mach 8.0, 2-D turbulent blunt wedge, computed wall heat flux.

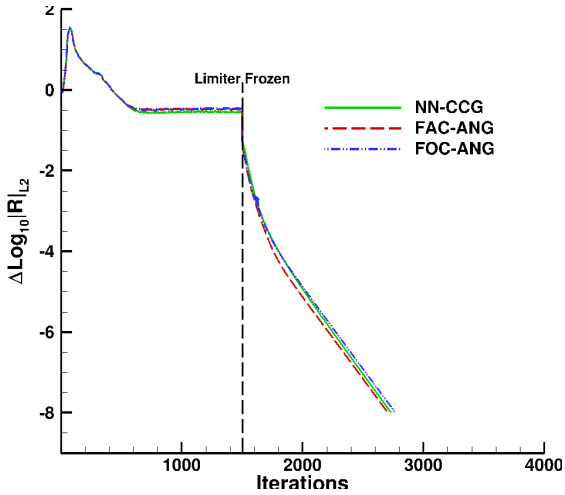

Fig. 22 Mach 8.0, 2-D turbulent blunt wedge, convergence behavior.

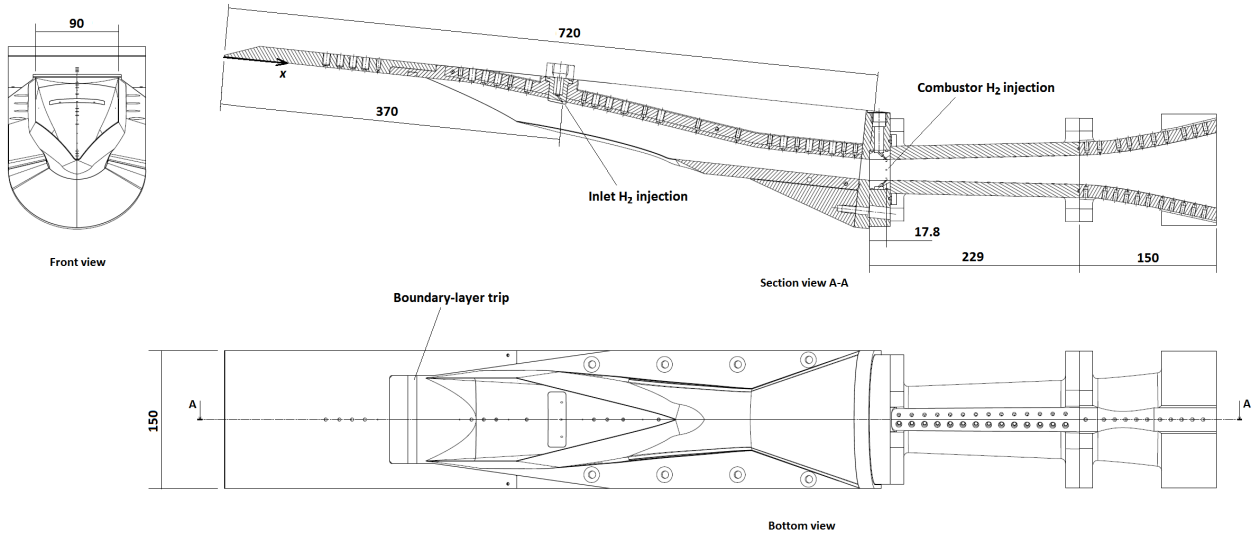

Fig. 23 Schematic of HIFiRE 7 REST scramjet engine experimental model as installed in the University of Queensland T4 Stalker Tube, at 0 degrees angle of attack relative to the combustor centerline, 6 degrees angle-of-attack relative to the forebody plate surface (the labeled x-axis).

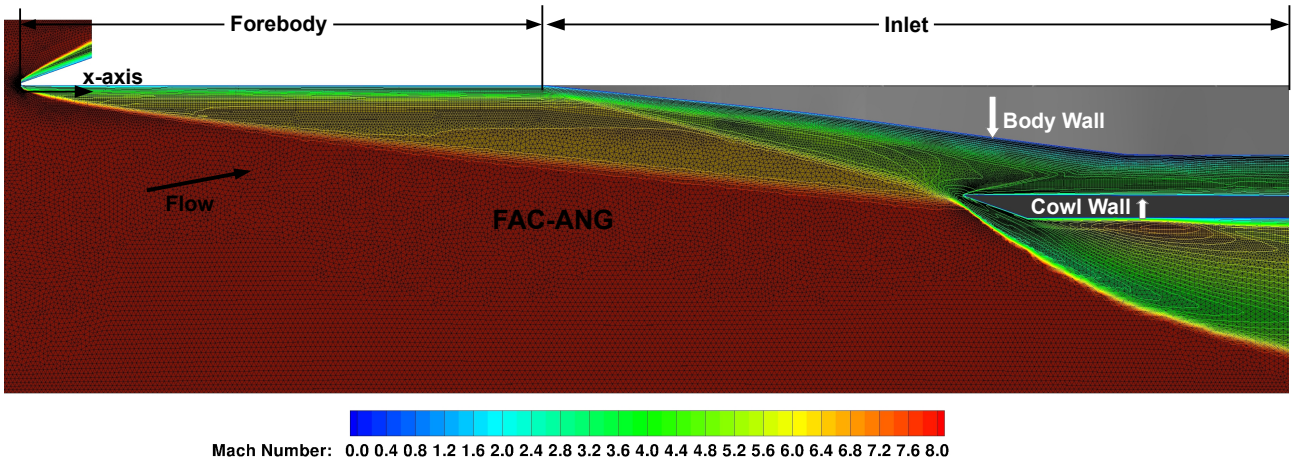

Fig. 24 HIFiRE 7 REST scramjet engine forebody/inlet symmetry plane computational Mach contours, with unstructured grid superimposed, showing the contours obtained using the FAC-ANG approach.

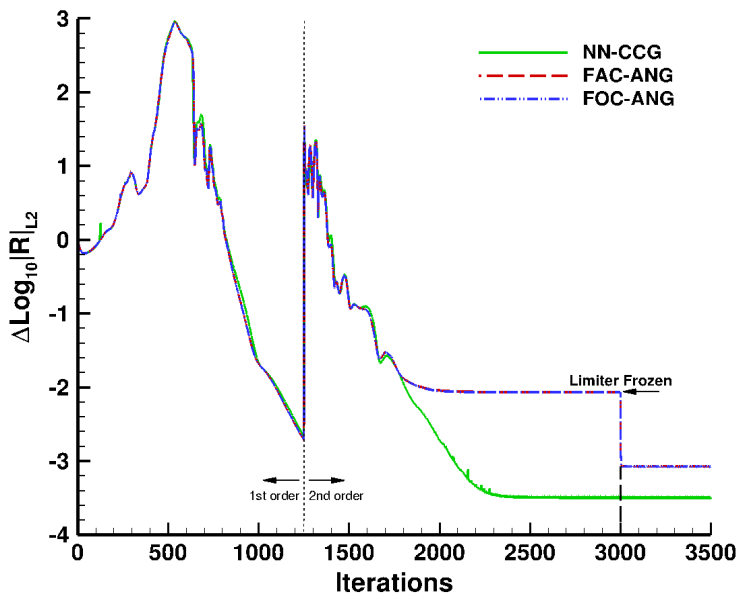

Fig. 25 A comparison of the residual convergence behavior for the HIFiRE 7 REST scramjet engine inlet using the NN-CCG, FAC-ANG and FOC-ANG approaches.

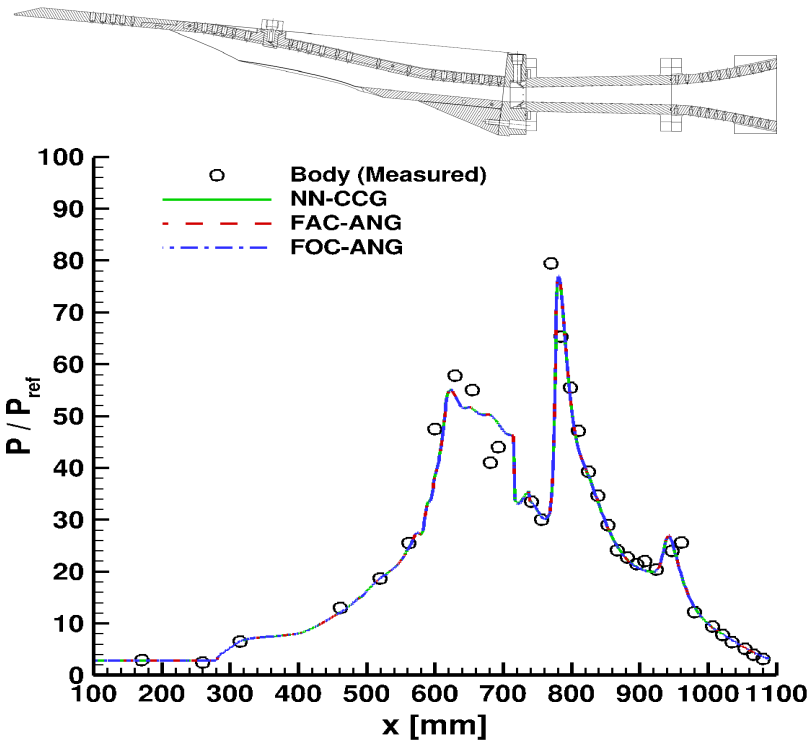

Fig. 26 A comparison of the computed HIFiRE 7 REST scramjet engine body wall center-line pressure distributions using the NN-CCG, FAC-ANG and FOC-ANG approaches with experimental data from Ref. [12].

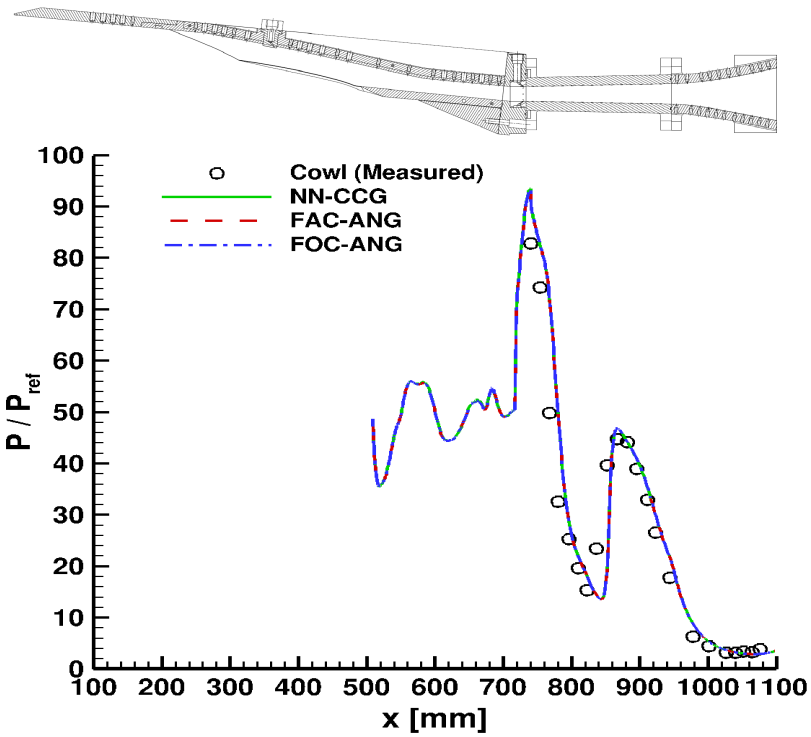

Fig. 27 A comparison of the computed HIFiRE 7 REST scramjet engine cowl wall center-line pressure distributions using the NN-CCG, FAC-ANG and FOC-ANG approaches with experimental data from Ref. [27].

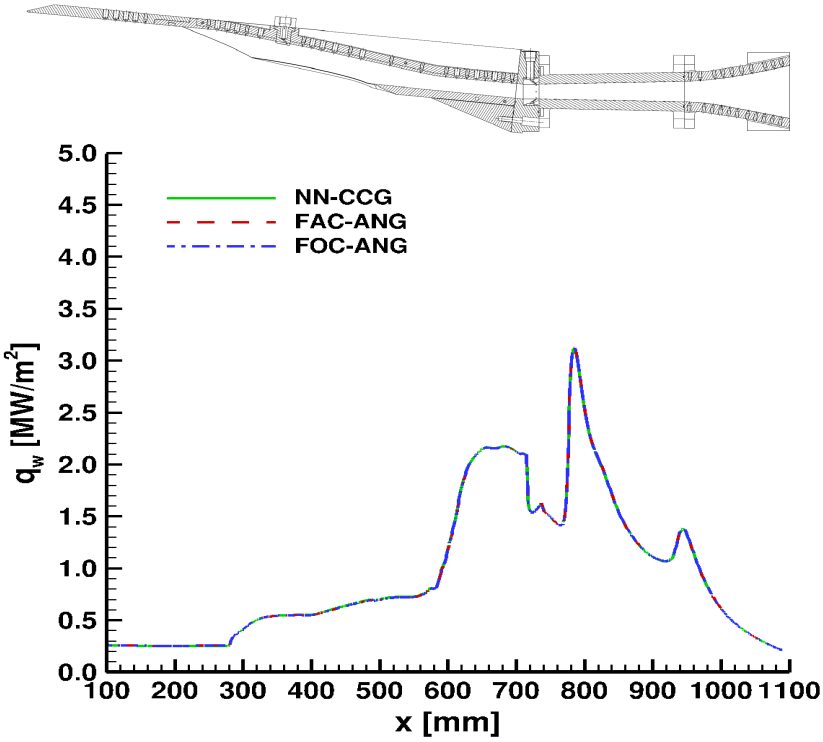

Fig. 28 A comparison of the computed HIFiRE 7 REST scramjet engine body wall center-line heat flux distribution using the NN-CCG, FAC-ANG and FOC-ANG approaches.

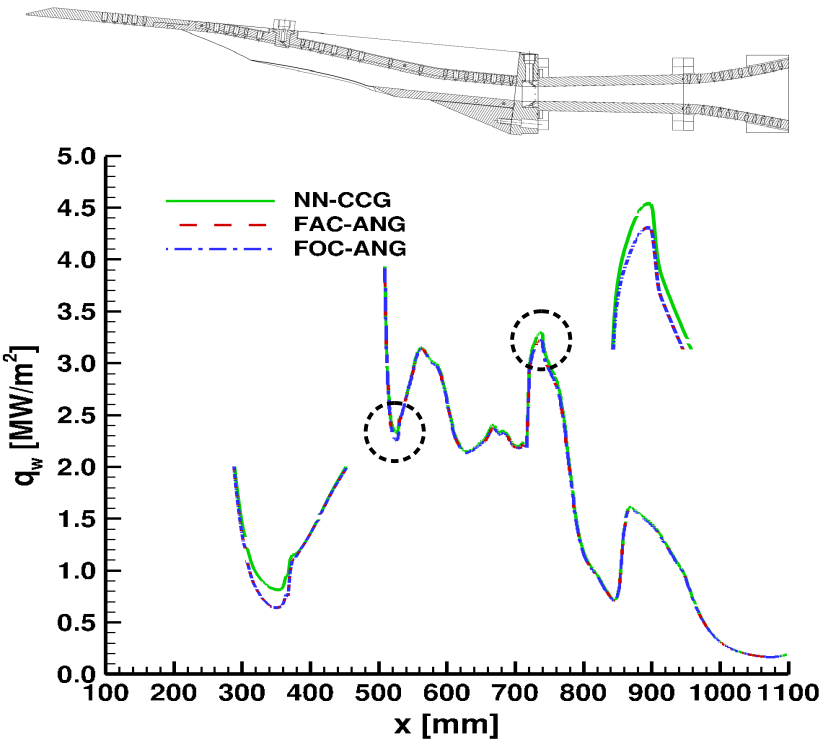

Fig. 29 A comparison of the computed HIFiRE 7 REST scramjet engine cowl wall center-line heat flux distribution using the NN-CCG, FAC-ANG and FOC-ANG approaches.

References

1. Park, M.A., Krakos, J.A., Michal, T, Loseille, A. and Alonso, J.J., "Unstructured Grid Adaptation: Status, Potential Impacts, and Recommended Investments Toward CFD Vision 2030," AIAA Paper 2016-3323, June 2016. doi:10.2514/6.2016-3323
2. Nishikawa, H. and White, J. A., "Face- and Cell-Averaged Nodal-Gradient Approach to Cell-Centered Finite-Volume Method on Mixed Grids," SciTech 2020 Forum, Orlando, FL, to be published as an AIAA Paper, January 2020.
3. Nishikawa, H. and White, J. A., "Face-Averaged Nodal-Gradient Approach to Cell-Centered Finite-Volume Method on Triangular Grids,", AIAA Paper 2019-3636, June 2019. doi:10.2514/6.2019-3636
4. White, J. A., Baurle, R. A., Passe, B. J., Spiegel, S. C. and Nishikawa, H., "Geometrically Flexible and Efficient Flow Analysis of High Speed Vehicles Via Domain Decomposition, Part 1, Unstructured-grid Solver for High Speed Flows," JANNAF 48th CS / 36th APS / 36th EPSS / 30th PSHS Joint Subcommittee / Programmatic and Industrial Base Meeting, Newport News, VA, Dec., 2017.
5. Nishikawa, H., "Efficient Gradient Stencils for Robust Implicit Finite-Volume Solver Convergence on Distorted Grids," *J. of Comput. Phys.*, Vol. 386, 2019, pp. 486-501. doi:10.1016/j.jcp.2019.02.026
6. White, J. A., Nishikawa, H., and Baurle, R. A., "Weighted Least-squares Cell-Average Gradient Construction Methods For The VULCAN-CFD Second-Order Accurate Unstructured-Grid Cell-Centered Finite-Volume Solver", AIAA Paper 2019-0127, January 2019. doi:10.2514/6.2019-0127
7. White, J. A., Baurle, R. A. and Nishikawa, H., "Efficient and Robust Weighted Least-squares Cell-Average Gradient Construction Methods for the Simulation of Scramjet Flows," JANNAF 49th CS / 37th APS / 37th EPSS / 31st PSHS Joint Subcommittee, Dayton, OH, June 2019.
8. Schwoppe, A. and Diskin, B., "Accuracy of the Cell-Centered Grid Metric in the DLR TAU-Code," *New Results in Numerical and Experimental Fluid Mechanics VIII. Notes on Numerical Fluid Mechanics and Multidisciplinary Design*, Vol. 121, 2013, Springer Berlin Heidelberg, pp. 429-437.
9. Sozer, E., Brehm, C. and Kiris, C. C., "Gradient Calculation Methods on Arbitrary Polyhedral Unstructured Meshes for Cell-Centered CFD Solvers," AIAA Paper 2014-1440, January 2014. doi:10.2514/6.2014-1440
10. Diskin, B. and Thomas, J. L., "Comparison of Node-Centered and Cell-Centered Unstructured Finite-Volume Discetizations: Inviscid Fluxes,"*AIAA Journal*, Vol. 49, No. 4, pp .836-854. doi:10.2514/1.J050897
11. Haider, F., Croiselle, J.-P., and Courbet, B., "Stability Analysis of the Cell Centered Finite-volume MUSCL Method on Unstructured Grids," *Numerische Mathematik*, Vol. 113, 2009, Springer Berlin Heidelberg, pp. 555-600.
12. Zangeneh, R. and Ollivier-Gooch, C. F., "Reconstruction Map Stability Analysis for Cell Centered Finite Volume Methods on Unstructured Meshes", AIAA Paper 2017-0734, January 2017. doi:10.2514/6.2017-0734
13. Zhang, F., Liu, J., Chen, B., and Zhong, W., "A Nodal-Weighted-Least-Squares Gradient Reconstruction for Cell-Centered Finite Volume Method," Unpublished, 2015.
14. Zhang, F., "A vertex-weighted-Least-Squares gradient reconstruction," arXiv:1702.04518 [physics.flu-dyn], 2017.
15. Zhang, F., "Research on Spatial Discretization Schemes for Finite Volume Method on Unstructured Grids," Ph.D. Thesis, Dalian University of Technology, 2017.
16. Frink, N. T., "Upwind Scheme for Solving the Euler Equations on Unstructured Tetrahedral Meshes," *AIAA Journal*, Vol., No. 1, January 1992, pp. 70-77. doi:10.2514/3.10884
17. Edwards, J. R., "A Low-Diffusion Flux-Splitting Scheme for Navier-Stokes Calculations," *Computers & Fluids,* Vol. 26, No. 6, 1997, pp. 635–659. doi:10.1016/S0045-7930(97)00014-5
18. Toro, E. F., Spruce, M., and Speares, W., "Restoration of the Contact Surface in the HLL-Riemann Solver," *Shock Waves,* Vol. 4, 1994, pp. 25–34.
19. Fromm, J. E., "A Method for Reducing Dispersion in Convective Difference Schemes," *Journal of Computational Physics*, Vol. 3, 1968, pp. 176–189.
20. Burg, C. O. E., "Higher-Order Variable Extrapolation for Unstructured Finite Volume RANS Flow Solvers," AIAA Paper 2005-4999, June 2005. doi:10.2514/6.2005-4999
21. Hasselbacher, A. and Blazek, J., "On the Accurate and Efficient Discretization of the Navier-Stokes Equations on Mixed Grids," AIAA Paper 1998-0612, January 1998. doi:10.2514/2.871
22. Diskin, B., Thomas, J. L., Nielsen, E., Nishikawa, H. and White, J. A., "Comparison of Node-Centered and Cell-Centered Unstructured Finite Volume Discretizations: Viscous Fluxes," *AIAA Journal*, Vol. 48, No. 7, 2010, pp. 1326–1339. doi:10.2514/1.44940
23. Jalai, A., Sharbtdar, M. and Ollivier-Gooch C., "Accuracy Analysis of Unstructured Finite Volume Discretization Schemes For Diffusive Fluxes," *Computers & Fluids*, Vol. 101, 2014, pp. 220–232. doi:10.1016/j.compfluid.2014.06.008
24. Nishikawa, H., "Beyond Interface Gradient: A General Principle for Constructing Diffusion Schemes," AIAA Paper 2010-5093, June 2010. doi:10.2514/6.2010-5093
25. Strang, G., *Linear Algebra and Its Applications*, Academic Press, 2nd ed., 1980.
26. Park, J. S. and Kim, C., "Multi-dimensional Limiting Process for Finite Volume Methods on Unstructured Grids," *Computers & Fluids*, Vol. 65, Elsevier Ltd, 2012, pp. 8–24. doi:10.1016/j.compfluid.2012.04.015
27. Chan, Y.K., Razzaqi, S. Smart, M.K. and Wise, D., "Freejet Testing of the 75%-scale HIFiRE 7 REST Scramjet Engine," AIAA Paper 2014-2931, June 2014. doi:10.2514/6.2014-2931
28. Wilcox, D. C., "Wall Matching, a Rational Alternative to Wall Functions," AIAA Paper 89-0611, January 1989.
29. Wilcox, D. C., "Formulation of the k-omega Turbulence Model Revisited," *AIAA Journal*, Vol. 46, No. 11, 2008, pp. 2823-2838. doi:10.2514/6.2007-1408
30. Wilcox, D. C., *Turbulence Modeling for CFD*, 2nd ed., DCW Industries, Inc., La Canada, CA, 1998, pp.121-122.
31. Menter, F. R., "Two-Equation Eddy-Viscosity Turbulence Models for Engineering Applications", *AIAA Journal,* Vol. 32, No. 8, 1994, pp. 1598–160. doi:10.2514/3.12149